



저작자표시-비영리-변경금지 2.0 대한민국

이용자는 아래의 조건을 따르는 경우에 한하여 자유롭게

- 이 저작물을 복제, 배포, 전송, 전시, 공연 및 방송할 수 있습니다.

다음과 같은 조건을 따라야 합니다:



저작자표시. 귀하는 원저작자를 표시하여야 합니다.



비영리. 귀하는 이 저작물을 영리 목적으로 이용할 수 없습니다.



변경금지. 귀하는 이 저작물을 개작, 변형 또는 가공할 수 없습니다.

- 귀하는, 이 저작물의 재이용이나 배포의 경우, 이 저작물에 적용된 이용허락조건을 명확하게 나타내어야 합니다.
- 저작권자로부터 별도의 허가를 받으면 이러한 조건들은 적용되지 않습니다.

저작권법에 따른 이용자의 권리는 위의 내용에 의하여 영향을 받지 않습니다.

이것은 [이용허락규약\(Legal Code\)](#)을 이해하기 쉽게 요약한 것입니다.

[Disclaimer](#)

공학박사 학위논문

**Applications of Carbon Functional Materials  
for Flexible Perovskite Solar Cells**

**유연 페로브스카이트 태양전지를 위한  
탄소기반 기능성 물질의 응용**

2019 년 8 월

서울대학교 대학원

기계항공공학부

윤 희 태

# **Applications of Carbon Functional Materials for Flexible Perovskite Solar Cells**

Heetae Yoon

School of Mechanical and Aerospace Engineering

The Graduate School

Seoul National University

## **Abstract**

Perovskite solar cell is the latest generation in the solar cell industry. Researchers in diverse areas paid attention to the debut of this new generation solar cell due to its great potential and fastest growth over the past few years. Unlike conventional silicon solar cells, the perovskite solar cell was able to integrate a flexible substrate and open its own industrial area. However, there was a materialistic limitation to move from a rigid substrate to a flexible substrate. The flexible substrates, such as PEN, was not able to withstand the high-temperature process of conventional transporting layer, such as TiO<sub>2</sub>. Also, a common transparent electrode, ITO, was suffering from price inflation

and its brittleness. In this dissertation, allotropes of carbon were introduced and optimized to integrate into flexible perovskite solar cells to replace conventional high-temperature processed transporting layers and high-cost brittle electrode.

First, a flexible stable perovskite with no hysteresis utilizing  $C_{60}$  as an electron transporting layer was realized and its stability was tested. To stabilize the transporting layer that caused major hysteresis and fabrication failure,  $C_{60}$  replaced conventional  $TiO_2$  electron transporting layer and eliminated bathocuproine layer to balance the band alignment of each layer within the perovskite solar cell. As a result, the  $C_{60}$  based flexible perovskite performed with PCE of 16.0%. For both rigid and flexible substrate, the  $C_{60}$  based flexible perovskite solar cell exhibited excellent stability by showing no hysteresis at a rapid scanning rate. Additionally, the PEN-based flexible device showed its durability over bending conditions. The cell maintained its performance over 90% after 1000 cycles of bending test with a radius of curvature of 10 mm. This study has set a new standard of stable flexible perovskite solar cell with promising results.

Second, a graphene-based hybrid electrode was realized to overcome the limitations of existing alternative transparent electrodes for flexible

optical devices. The combination of graphene and Ag NW led a self-complementary condition that enhances each other's limitations with the help of amorphous Teflon backbone polymer layer. Graphene enlarged its size limitations by enhancing its conductivity with help of a super thin layer of Ag NW. Ag NW was able to protect its own layer with help of graphene to enhance its chemical stability over any chemicals including organic solvents. Both graphene and Ag NW are suitable for flexibility and showed similar transparency and conductivity as that of ITO. Unlike ITO, the transparency and conductivity of this hybrid electrode are controllable. The roughness of the hybrid electrode was very flat with under 5 nm of roughness rms. The surface treatment with PFN enhanced the surface compatibility with other chemicals. The hybrid electrode showed its compatibility in both spin-coating and mega-sonic spray deposition. This study has shown the potential of the graphene-based hybrid electrode and its accessibility to be integrated into other optical and energy-related research area.

Overall the studies have shown the advantage over the most abundant material on earth, carbon. Carbon and its allotropes can replace major parts of perovskite solar cells excluding the active layer,

perovskite. Its potential of stabilizing perovskite solar cell is expected to strengthen the possibility of the production of industrial flexible perovskite solar cell. Moreover, the introduction of a new hybrid electrode that can potentially replace ITO and stop the monopoly of indium price war should open a new area of studies with its superb flexibility.

**Keywords:** perovskite solar cells, flexible device, carbon, C<sub>60</sub>, graphene, hysteresis, transparent electrode

**Student Number:** 2013-20689

# Contents

<b>Abstract</b> .....	<b>i</b>
<b>Contents</b> .....	<b>v</b>
<b>List of Tables</b> .....	<b>vii</b>
<b>List of Figures</b> .....	<b>viii</b>
<b>Chapter 1. Introduction</b> .....	<b>1</b>
1.1. Research Background .....	1
1.2. Research Objectives.....	5
1.3. References.....	7
<b>Chapter 2. Introduction to Flexible Perovskite Solar Cell</b> .....	<b>13</b>
2.1. Solar Cell Performnace Parameters .....	13
2.2. Transporting Layer in Flexible Perovskite Solar Cell .....	16
2.2.1. Overview of Transporting Layer for Perovskite Solar Cell	16
2.3. Electrodes for Flexible Perovskite Solar Cell .....	19
2.3.1. Overview of Non-ITO Transparent Electrode .....	16
2.3.2. Selecting Stable Polymer Substrate for Flexible Electrodes .....	23
2.4. References.....	28
<b>Chapter 3. Hysteresis-free Flexible Perovskite Solar Cell</b> <b>by Utilizing C<sub>60</sub> as Electron Transporting Layer .....</b>	<b>32</b>
3.1. Introduction.....	32
3.2. Experimental Methods.....	37

3.2.1.	Fabrication of Perovskite Solar Cells .....	37
3.2.2.	Characterization .....	40
3.3.	Results and Discussion .....	42
3.3.1.	Structure of C <sub>60</sub> -based PSC.....	42
3.3.2.	Elimination of BCP Hole Blocking Layer .....	46
3.3.3.	C <sub>60</sub> Optimization .....	50
3.3.4.	Performance of PSC.....	56
3.3.5.	Performance of flexible PSC .....	60
3.4.	Conclusion .....	64
3.5.	References.....	65

## **Chapter 4. Graphene-based Hybrid Electrode for Flexible Electronics ..... 71**

4.1.	Introduction.....	71
4.2.	Experimental Methods.....	75
4.2.1.	Synthesis of Ag NW .....	75
4.2.2.	Synthesis of 2L Graphene/Cu film.....	77
4.2.3.	Fabrication of Hybrid Electrode .....	78
4.2.4.	Fabrication of Perovskite Solar Cell .....	80
4.2.5.	Characterization .....	82
4.3.	Results and Discussion .....	83
4.3.1.	Structure of the Hybrid Electrode Based Solar Cell .....	83
4.3.2.	Teflon Optimization.....	87
4.3.3.	Conductivity and Transparency Optimization .....	98
4.3.4.	Characterization of Hybrid Electrode .....	101
4.3.5.	Surface Compatibility Enhancement .....	106

4.4.	Conclusion .....	110
4.5.	References.....	111
	<b>Chapter 5. Conclusion .....</b>	<b>116</b>
	<b>Acknowledgement .....</b>	<b>119</b>
	<b>Abstract (in Korean) .....</b>	<b>120</b>
	<b>List of Publications.....</b>	<b>123</b>

## List of Tables

Table 2.1 List of transparent polymer candidate for Ag NW embedding. Each material was tested with organic solvent to compare its chemical resistivity toward perovskite fabrication. ....	26
Table 3.1 Statistical results of the performance of the perovskite solar cells on glass/ITO substrate employing C <sub>60</sub> electron transporting layer .....	58
Table 3.2 Summary of the average performance of the CH <sub>3</sub> NH <sub>3</sub> PbI <sub>3</sub> perovskite devices incorporating C <sub>60</sub> layer on flexible substrate. ....	63
Table 4.1 Sheet resistance for each type of electrodes.....	100
Table 4.2 Statistical data from AFM measurement for hybrid electrode and ITO. Unlike ITO, the hybrid electrode do show difference between mid and mean value, but the values are still under 10 nm, confirming its flatness.....	104

## List of Figures

Figure 2.1 Current density-voltage(J-V) curve of perovskite solar cell .....	15
Figure 2.2 Transferred Ag NW on glass substrate with partial passivation by graphene layer. The sample was left for 40 days in ambient condition. Ag NW with graphene passivation stayed transparent while the other part of Ag NW was oxidized and turned yellow.....	21
Figure 2.3 The cross-sectional SEM image of (a) normal perovskite solar cell structure with evaporated C <sub>60</sub> layer as ETL and (b) inverted perovskite solar cell structure with spin-coated PEDOT:PSS layer as HTL. Transporting layer with evaporation deposition method had discontinuity while that of spin-coating method had very poor uniformity.....	22
Figure 2.4 Conceptual structure of graphene Ag NW composite on glass substrate and embedding in transparent polymer. ....	26
Figure 2.5 Graphical results for cPI and PI chemical resistivity test. Each sample is tested with organic solvent such as DMF and DMSO. The result is shown with red marks: X and triangle indicate total and partial failure and O indicates success. The sample condition is listed as the following: (a) bare cPI, (b) cPI with evaporated C <sub>60</sub> , (c) cPI with evaporated molybden oxide, (d) cPI with spin-coated nickel oxide nanoparticle, (e) cPI with spin-coated PEDOT:PSS, and (f) normal PI layer as a reference sample.. ....	27
Figure 3.1 The progress of perovskite solar cell structure from (a-c) DSSC and from (d-e) OPV to utilize flexible substrate.....	44
Figure 3.2 (a) the structure of perovskite solar cell and (b) the relative energy level diagram of the MAPbI <sub>3</sub> perovskite solar cell adapting C <sub>60</sub> as ETL with or without BCP layer. Red marks on both images indicate the BCP elimination.....	45

Figure 3.3 (a) J-V curves of the devices adapting C <sub>60</sub> layer with and without BCP layer (b,c) The Nyquist plots of planar heterojunction perovskite solar cells adapting C <sub>60</sub> layer with and without BCP layer.....	49
Figure 3.4 Variation in the transmittance of C <sub>60</sub> /ITO/Glass with different thickness of C <sub>60</sub> layer from 0 nm to 35 nm.....	53
Figure 3.5 (a-e) Cross-sectional SEM images of the devices with different C <sub>60</sub> thickness. Minimum thickness of 30 nm is required for C <sub>60</sub> deposition to have a uniform layer that covers the surface. Optimum thickness is 35 nm with best performance.....	54
Figure 3.6 (a) Open circuit voltage ( <i>V<sub>OC</sub></i> ), (b) fill factor, (c) current density ( <i>J<sub>SC</sub></i> ), (d) PCE, (e) shunt resistance, and (f) series resistance comparison with different C <sub>60</sub> thickness. ....	55
Figure 3.7 (a) J-V characteristics of the MAPbI <sub>3</sub> perovskite cells measured at forward scan and reverse scan with various dwelling time (20 ms to 800 ms) at 20 mV per step (b) EQE profile and integrated photocurrent density of the best performing device.....	58
Figure 2.8 Steady-state photocurrent measurement of the fabricated planar perovskite solar cell for 10 min at 0.82 V, which corresponds to the maximum power point. The inset shows current response of devices switched from open-circuit to short-circuit under illumination. ....	59
Figure 3.9 (a) The structure of flexible MAPbI <sub>3</sub> perovskite solar cell on a PEN/ITO substrate. (b) Cross sectional FE-SEM Image of a flexible MAPbI <sub>3</sub> perovskite solar cell (c) J-V characteristics of the perovskite cell. The Inset shows a digital camera image of the fabricated MAPbI <sub>3</sub> perovskite solar cell (d) Efficiency of flexible perovskite devices as a function of bending cycles with different radii of 10 mm and 5 mm. R <sub>b</sub> is the radius of curvature. ....	62
Figure 4.1 The structure of the hybrid electrode and flexible perovskite solar cell on	

the hybrid electrode. ....	85
Figure 4.2 Chemical equation comparison for amorphous Teflon and normal Teflon... .....	90
Figure 4.3 Schematic image of bubbly cured Teflon surface and its alternative process to easily detach Teflon layer by applying PMMA sacrificial layer.....	91
Figure 4.4 Schematic image of transferred Teflon layer with bubbly surface and its following fabrication process effects due to its bubbly surface.....	92
Figure 4.5 Photographic image of the top surface of fabricated solar cell on bumpy Teflon layer. The surface morphology shows wavy top layer that is caused by the bumpy surface occurred during Teflon curing.....	93
Figure 4.6 Schematic process of fabrication of the hybrid electrode. CVD processed graphene on copper foil was attached on rigid glass followed by Ag NW and AF Teflon deposition through spin-coating method. Then, primer is coated on the surface of Teflon layer to attach final substrate, PEN or glass. The hybrid electrode is detached from initial glass substrate. Copper foil is removed in metal etchant bath.....	95
Figure 4.7 Photographic image of the hybrid electrode on (a) 40 mm X 40 mm flexible substrate and (b) 25 mm X 25 mm flexible substrate. ....	97
Figure 4.8 (a) Transmittance and (sheet resistance) comparison for different concentration of Ag NW. The transmittance and sheet resistance are inversely proportional to each other. Ag NW of 0.1 wt% is used since the sheet resistance of 0.1 wt% is the closest to that of ITO. ....	99
Figure 4.9 Transmittance comparison for different electrode materials. For Ag NW and hybrid electrode, 0.1 wt% of Ag NW was used. The average transmittance results between 350 nm ~ 800 nm for ITO, Ag NW, and hybrid electrode are 91.18%, 90.97%, and 87.1% respectively.....	100
Figure 4.10 Surface SEM image of the hybrid electrode on flat and 30° tilted angle.	

The contrast between two images and the contrast within the same image is very minimal and implies Ag NW is perfectly embedded inside the polymer..... 103

Figure 4.11 AFM images of both (a) hybrid electrode and (b) ITO. The hybrid electrode do show wrinkles on the surface, but overall the flatness is confirmed and Ag NW is untraceable..... 104

Figure 4.12 Increase in resistance versus number of bends for the hybrid electrode and ITO electrode on PEN substate due to (a) 10 mm and (b) 5 mm bending radius ..... 104

Figure 4.13 Visual data of surface treatment with PFN on the hybrid electrode. The contact angle of the hybrid electrode decreased from (a) 110° to (b) 93°. (c) and (d) compares the visual after dripping organic solvent on the hybrid electrode. The surface treatment enabled further perovskite fabrication on the hybrid electrode. .... 108

Figure 4.14 Cross-sectional SEM image for ITO and hybrid electrodes after full perovskite cell fabrication. PFN treatment successfully enabled perovskite layer fabrication through both spin-coating and spray methods. .... 109

## Nomenclature

$J_{SC}$	Short-circuit current density	[mA cm <sup>-2</sup> ]
$V_{OC}$	Open-circuit voltage	[V]
$FF$	Fill factor	[%]
$PCE$	Power conversion efficiency	[%]
$EQE$	External quantum efficiency	[%]
$r_b$	Bending radius	[mm]
$R_{SC}$	Shunt resistance	[ohm cm <sup>-2</sup> ]
$R_S$	Series resistance	[ohm cm <sup>-2</sup> ]

# Chapter 1. Introduction

---

## 1.1. Research Background

Perovskite Solar Cell is a type of solar cell which includes perovskite structured material as light absorbing layer. Perovskite structure refers to any material with same type of crystal structure as  $\text{CaTiO}_3$ , or commonly known as  $\text{ABX}_3$ . Perovskite absorbing layer is an organic-inorganic material based on organic cation ( $\text{CH}_3\text{NH}_3^+$  or  $\text{NC}(\text{NH}_2)_2^+$ ) as 'A', metal (Pb or Sn) as 'B', and halogen anion ( $\text{Br}^-$ ,  $\text{Cl}^-$ , or  $\text{I}^-$ ) as 'X' in  $\text{ABX}_3$  structure [1,2]. The organic-inorganic metal halide perovskite has high absorption coefficient that can absorb most of visible solar spectrum along with balanced electron/hole mobility, smaller exciton binding energy, and longer exciton diffusion length than previous organic materials [3-8]. The fabrication methods for perovskite film can be done through vacuum process or solution process, which are both done under low-temperature ( $<150^\circ\text{C}$ ) condition [8,9]. Due to its low cost fabrication and relatively cheap raw materials, Perovskite Solar Cell has opened its own unique area to

various researchers and engineers especially to those in flexible device area [10-13]. The efficiencies of Perovskite Solar Cell have increased from 3.8% in 2009 to 23.3% in 2018 [14]. It is the fastest advancing solar technology to date.

The structure of perovskite solar cell comes from two different roots: Dye-sensitized solar cell (DSSC) and organic photovoltaic (OPV) solar cell. DSSC uses mesoporous  $\text{TiO}_2$  layer to maximize the surface to volume ratio to efficiently extract the excitons from the active layer. The identical transporting layer,  $\text{TiO}_2$ , is successfully adopted in perovskite solar cells elevating its efficiency over 20% [15-17]. The high-temperature process required for mesoporous  $\text{TiO}_2$  enhances the performance of perovskite solar cell, but the material characteristics caused electrical hysteresis and usage limitation due to high-temperature process. OPV uses multi-layer of transporting and blocking layers to optimize the band alignment of the device [18-21]. Due to low mobility characteristics of most organic materials, most organic layers are ultra-thin layer and is optimized for planar cell structures. To improve the performance of flexible perovskite solar cell, utilizing and optimizing organic transporting layers are very essential due to its low-temperature processability.

Despite its limitations regarding transporting materials, there have been improvements in flexible perovskite solar cells [22-27]. However, indium tin oxide (ITO) or fluorine doped tin oxide (FTO), most commonly used conductive oxide transparent electrodes in optoelectronics, hinder the process due to their brittle nature of ceramic making it incompatible [29].

To overcome the limitations, allotropes of pure carbon can be used to replace transporting layers and transparent electrodes. Carbon is one of the few elements known since antiquity. It is the 15<sup>th</sup> most abundant element in the Earth's crust, and the fourth most abundant element in the universe by mass after hydrogen, helium, and oxygen [30,31]. Carbon is capable of forming many allotropes due to its valency. In recent decades many allotropes have been discovered and researched including ball shapes such as buckminsterfullerene and sheets such as graphene.

Fullerenes such as phenyl-C<sub>61</sub>-butyric acid methyl ester (PCBM) and C<sub>60</sub> [32-34] have been used as the ETL in perovskite solar cells because they are known to reduce the density of trap states and passivate the grain boundaries of methylammonium lead iodide (CH<sub>3</sub>NH<sub>3</sub>PbI<sub>3</sub>) absorbing layer [34,35]. In addition, the C<sub>60</sub> can be

packed more densely than PCBM to facilitate intermolecular charge transport, and shows much higher electron mobility ( $1.6 \text{ cm}^2/\text{V}\cdot\text{s}$ ) and conductivity ( $2.3 \times 10^{-3} \text{ S/cm}$ ) compared to the PCBM ( $6.1 \times 10^{-2} \text{ cm}^2/\text{V}\cdot\text{s}$  and  $3.2 \times 10^{-4} \text{ S/cm}$ , respectively) [36]. Thus  $\text{C}_{60}$  is a good candidate for an electron transporting layer (ETL) in perovskite solar cells through vacuum process. Although the  $\text{C}_{60}$  starts to evaporate at over  $400^\circ\text{C}$ , the substrate does not heat up due to lack of medium to transport the heat from source,  $\text{C}_{60}$ , to the substrate target, enabling low-temperature process.

Graphene is well known dream material for its expert electrical and mechanical properties. Graphene alone can be applied as transparent electrode. There is a size limitation due to defects from wet/dry transfers [28,29]. Graphene can form a composite material with Ag NW to form a hybrid electrode that exceeds size limitations. The Ag NW sustains high conductivity while remaining its long-term stability through graphene passivation cover. Both Ag NW and graphene is capable of flexible and even foldable electrode with high transmittance.

## 1.2. Research Objectives

This dissertation aims to improve overall performance of flexible PSCs by introducing carbon-based applied materials as alternative layers for ETLs and electrodes layers. Chapter 1 and Chapter 2 covers an introduction of this dissertation, which provides the background and objective of the research.

In chapter 3, we introduce vacuum-processed  $C_{60}$  Buckminsterfullerene to eliminate the photocurrent hysteresis and high-temperature processed ETLs. By optimizing the thickness of  $C_{60}$  layer, the highly homogeneous, uniform, and dense  $C_{60}$  layer passivates the surfaces of the perovskite layer and enhances charge transport property. As a result,  $C_{60}$  layer eliminates the photocurrent hysteresis and improves overall performance of the solar cell. For the first time, we apply vacuum-processed  $C_{60}$  on polyethylene naphthalate (PEN) substrate to demonstrate a hysteresis-free flexible perovskite solar cell with 16% efficiency.

In chapter 4, we introduce a graphene based hybrid transparent electrode as a solution to current size limitation of graphene electrode. By utilizing graphene with embedded Ag NW, the hybrid electrode

enables large area fabrication along with promising sheet resistance that performs like ITO. The hybrid electrode is chemically very stable and is applicable to any materials. Also the surface treatment enhanced the adhesion of hydrophobic surface of graphene, overcoming the fabrication limitation such as spin-coating.

In chapter 5, the work presented in this dissertation is summarized and their future work is suggested.

### 1.3. References

- [1] M. A. Green, A. Ho-Baillie, H. J. Snaith, The emergence of perovskite solar cells, *Nature Photonics*, 8, 506-514 (2014)
- [2] J.-P. Correa-Baena, A. Abate, M. Saliba, W. Tress, T. J. Jacobsson, M. Grätzel, A. Hagfeldt, The rapid evolution of highly efficient perovskite solar cells, *Energy & Environmental Science*, 10, 710-727 (2017)
- [3] Lee, M. M., Teuscher, J., Miyasaka, T., Murakami, T. N., & Snaith, H. J. (2012). Efficient hybrid solar cells based on meso-superstructured organometal halide perovskites. *Science*, 338(6107), 643-647.
- [4] Shi, D., Adinolfi, V., Comin, R., Yuan, M., Alarousu, E., Buin, A., . . . Katsiev, K. (2015). Low trap-state density and long carrier diffusion in organolead trihalide perovskite single crystals. *Science*, 347(6221), 519-522.
- [5] Stranks, S. D., Eperon, G. E., Grancini, G., Menelaou, C., Alcocer, M. J., Leijtens, T., . . . Snaith, H. J. (2013). Electron-hole diffusion lengths exceeding 1 micrometer in an organometal trihalide perovskite absorber. *Science*, 342(6156), 341-344.
- [6] Sung, H., Ahn, N., Jang, M. S., Lee, J. K., Yoon, H., Park, N. G., & Choi, M. (2016). Transparent Conductive Oxide-Free Graphene-Based Perovskite Solar Cells with over 17% Efficiency. *Advanced Energy Materials*, 6(3), 1501873.
- [7] Xing, G., Mathews, N., Sun, S., Lim, S. S., Lam, Y. M., Grätzel, M., . . . Sum, T. C. (2013). Long-range balanced electron-and hole-

- transport lengths in organic-inorganic CH<sub>3</sub>NH<sub>3</sub>PbI<sub>3</sub>. *Science*, 342(6156), 344-347.
- [8] Li, X., Bi, D., Yi, C., Décoppet, J. D., Luo, J., Zakeeruddin, S. M., ... & Grätzel, M. (2016). A vacuum flash-assisted solution process for high-efficiency large-area perovskite solar cells. *Science*, 353(6294), 58-62.
- [9] Ahn, N., Son, D. Y., Jang, I. H., Kang, S. M., Choi, M., & Park, N. G. (2015). Highly reproducible perovskite solar cells with average efficiency of 18.3% and best efficiency of 19.7% fabricated via Lewis base adduct of lead (II) iodide. *Journal of the American Chemical Society*, 137(27), 8696-8699.
- [10] Burschka, J., Pellet, N., Moon, S.-J., Humphry-Baker, R., Gao, P., Nazeeruddin, M. K., & Grätzel, M. (2013). Sequential deposition as a route to high-performance perovskite-sensitized solar cells. *Nature*, 499(7458), 316.
- [11] Dong, Q., Fang, Y., Shao, Y., Mulligan, P., Qiu, J., Cao, L., & Huang, J. (2015). Electron-hole diffusion lengths > 175 μm in solution-grown CH<sub>3</sub>NH<sub>3</sub>PbI<sub>3</sub> single crystals. *Science*, 347(6225), 967-970.
- [12] Gong, J., Darling, S. B., & You, F. (2015). Perovskite photovoltaics: life-cycle assessment of energy and environmental impacts. *Energy & Environmental Science*, 8(7), 1953-1968.
- [13] Jung, H. S., & Park, N. G. (2015). Perovskite solar cells: from materials to devices. *small*, 11(1), 10-25.
- [14] [http://www.nrel.gov/ncpv/images/efficiency\\_chart.jpg](http://www.nrel.gov/ncpv/images/efficiency_chart.jpg)

- [15] Zhou, H., Chen, Q., Li, G., Luo, S., Song, T. B., Duan, H. S., ... & Yang, Y. (2014). Interface engineering of highly efficient perovskite solar cells. *Science*, 345(6196), 542-546.
- [16] Tao, C., Neutzner, S., Colella, L., Marras, S., Kandada, A. R. S., Gandini, M., ... & Bertarelli, C. (2015). 17.6% stabilized efficiency in low-temperature processed planar perovskite solar cells. *Energy & Environmental Science*, 8(8), 2365-2370.
- [17] Snaith, H. J., Abate, A., Ball, J. M., Eperon, G. E., Leijtens, T., Noel, N. K., ... & Zhang, W. (2014). Anomalous hysteresis in perovskite solar cells. *J. Phys. Chem. Lett*, 5(9), 1511-1515.
- [18] Ke, W., Zhao, D., Grice, C. R., Cimaroli, A. J., Ge, J., Tao, H., ... & Yan, Y. (2015). Efficient planar perovskite solar cells using room-temperature vacuum-processed C 60 electron selective layers. *Journal of Materials Chemistry A*, 3(35), 17971-17976.
- [19] Cao, W., & Xue, J. (2014). Recent progress in organic photovoltaics: device architecture and optical design. *Energy & Environmental Science*, 7(7), 2123-2144.
- [20] Xue, J., Uchida, S., Rand, B. P., & Forrest, S. R. (2004). Asymmetric tandem organic photovoltaic cells with hybrid planar-mixed molecular heterojunctions. *Applied Physics Letters*, 85(23), 5757-5759.
- [21] Pfuetzner, S., Meiss, J., Petrich, A., Riede, M., & Leo, K. (2009). Improved bulk heterojunction organic solar cells employing C 70 fullerenes. *Applied Physics Letters*, 94(22), 145.
- [22] Kim, H. S., Lee, C. R., Im, J. H., Lee, K. B., Moehl, T., Marchioro, A., ... & Grätzel, M. (2012). Lead iodide perovskite sensitized all-

- solid-state submicron thin film mesoscopic solar cell with efficiency exceeding 9%. *Scientific reports*, 2, 591.
- [23] Yang, W. S., Park, B. W., Jung, E. H., Jeon, N. J., Kim, Y. C., Lee, D. U., ... & Seok, S. I. (2017). Iodide management in formamidinium-lead-halide-based perovskite layers for efficient solar cells. *Science*, 356(6345), 1376-1379.
- [24] Gheno, A., Huang, Y., Bouclé, J., Ratier, B., Rolland, A., Even, J., & Vedraïne, S. (2018). Toward Highly Efficient Inkjet-Printed Perovskite Solar Cells Fully Processed Under Ambient Conditions and at Low Temperature. *Solar RRL*, 2(11), 1800191.
- [25]Ciro, J., Mejía-Escobar, M. A., & Jaramillo, F. (2017). Slot-die processing of flexible perovskite solar cells in ambient conditions. *Solar Energy*, 150, 570-576.
- [26]Barrows, A. T., Pearson, A. J., Kwak, C. K., Dunbar, A. D., Buckley, A. R., & Lidzey, D. G. (2014). Efficient planar heterojunction mixed-halide perovskite solar cells deposited via spray-deposition. *Energy & Environmental Science*, 7(9), 2944-2950.
- [27]Das, S., Yang, B., Gu, G., Joshi, P. C., Ivanov, I. N., Rouleau, C. M., ... & Xiao, K. (2015). High-performance flexible perovskite solar cells by using a combination of ultrasonic spray-coating and low thermal budget photonic curing. *Acs Photonics*, 2(6), 680-686.
- [28]Sung, H., Ahn, N., Jang, M. S., Lee, J. K., Yoon, H., Park, N. G., & Choi, M. (2016). Transparent Conductive Oxide-Free Graphene-Based Perovskite Solar Cells with over 17% Efficiency. *Advanced Energy Materials*, 6(3), 1501873

- [29] Yoon, J., Sung, H., Lee, G., Cho, W., Ahn, N., Jung, H. S., & Choi, M. (2017). Superflexible, high-efficiency perovskite solar cells utilizing graphene electrodes: towards future foldable power sources. *Energy & Environmental Science*, 10(1), 337-345.
- [30] Anderson, Don L.; 'Chemical Composition of the Mantle' in *Theory of the Earth*, pp. 147-175
- [31] Crosswell, Ken (February 1996). *Alchemy of the Heavens*. Anchor. ISBN 0-385-47214-5.
- [32] Heo, J. H., Han, H. J., Kim, D., Ahn, T. K., & Im, S. H. (2015). Hysteresis-less inverted CH<sub>3</sub>NH<sub>3</sub>PbI<sub>3</sub> planar perovskite hybrid solar cells with 18.1% power conversion efficiency. *Energy & Environmental Science*, 8(5), 1602-1608.
- [33] Liu, Y., Bag, M., Renna, L. A., Page, Z. A., Kim, P., Emrick, T., ... & Russell, T. P. (2016). Understanding interface engineering for high-performance fullerene/perovskite planar heterojunction solar cells. *Advanced Energy Materials*, 6(2), 1501606.
- [34] Shao, Y., Xiao, Z., Bi, C., Yuan, Y., & Huang, J. (2014). Origin and elimination of photocurrent hysteresis by fullerene passivation in CH<sub>3</sub>NH<sub>3</sub>PbI<sub>3</sub> planar heterojunction solar cells. *Nature communications*, 5, 5784.
- [35] Abrusci, A., Stranks, S. D., Docampo, P., Yip, H. L., Jen, A. K. Y., & Snaith, H. J. (2013). High-performance perovskite-polymer hybrid solar cells via electronic coupling with fullerene monolayers. *Nano letters*, 13(7), 3124-3128.
- [36] Liang, P. W., Chueh, C. C., Williams, S. T., & Jen, A. K. Y. (2015). Roles of fullerene-based interlayers in enhancing the performance

of organometal perovskite thin-film solar cells. *Advanced Energy Materials*, 5(10), 1402321.

## Chapter 2.

# Introduction to Flexible Perovskite Solar Cell

---

### 2.1. Solar Cell Performance Parameters

The performance of the solar cell can be characterized by 4 main factors: open-circuit voltage ( $V_{OC}$ ), short circuit current density ( $J_{SC}$ ), fill factor (FF), and maximum power conversion efficiency (PCE). The value of each parameter in J-V curve is shown in Figure 2.1.

The J-V curve of a perovskite solar cell is the superposition of the J-V curve of the perovskite solar cell diode in the dark with the light-generated current. The light shifts the J-V curve toward the second quadrant where power can be extracted from the maximum area under the curve. The short circuit current density ( $J_{SC}$ ) is the current density of the device under 1 sun illumination, when external field is not applied ( $V = 0$  V). The current density is determined by how many carriers are generated and extracted under 1 sun illumination. In other words, the

current density is related to the optical and electrical properties of the perovskite solar cell. The optical property reflects the amount of light absorption, which is determined by the band gap. While the electrical property determines various factors from transporting mobility and donor/acceptor phase separation to recombination and extraction/collection. As a result, it is critical to optimize both optical and electrical aspects of the device for maximum performance.

The open circuit voltage ( $V_{OC}$ ) is the voltage where the current density is zero ( $J_{SC} = 0 \text{ mA/cm}^2$ ). This occurs when the amount of injected carriers matches the amount of photo-generated carriers. The  $V_{OC}$  is proportional to the band gap of the perovskite absorbing layer. Efficient band alignment with transporting layer insures high open circuit voltage. The loss of the open circuit voltage is mainly due to traps and recombination within the device.

The maximum power point is the point where the multiplication of the current density and open circuit voltage is maximized. The maximum power point is also used to determine the fill factor (FF). Fill factor is the ratio between  $V_{max} \times J_{max}$  and  $V_{OC} \times J_{SC}$ . In other words, if the ideal device with no loss can be fabricated, the fill factor would be 1, since there is no leakage current nor losses.

The maximum power efficiency (PCE) is defined as the ratio of energy output from the solar cell to input energy from the sun. it is determined as the function of incident power which is converted to electricity. Power efficiency is the product of  $V_{OC}$ ,  $J_{SC}$ , and FF. Graphically, it is the area of the maximum rectangle under the curve in figure 2.1.

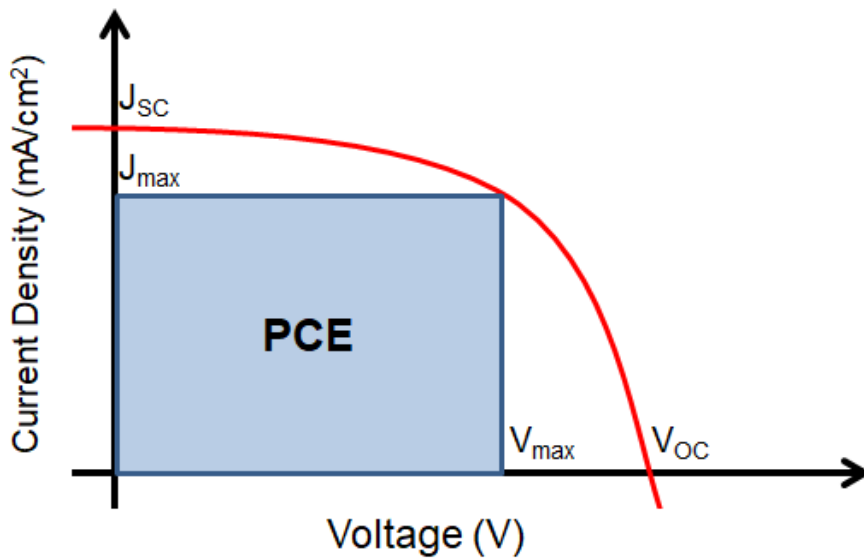


**Figure 2.1** Current density-voltage (J-V) curve of perovskite solar cell

## **2.2 Transporting Layer in Flexible Perovskite Solar Cell**

### **2.3.1. Overview of Transporting Layer for Perovskite Solar Cell**

The perovskite solar cells with high performances have usually adopted the n-i-p architecture, commonly using TiO<sub>2</sub> material as an electron transport layer (ETL) [1-4]. Here the TiO<sub>2</sub> compact layer requires a high-temperature process over 450 °C, which precludes its application on flexible substrates. To solve this limitation, low-temperature solution-processed TiO<sub>2</sub> has been used as the ETL [5-7]. However, the serious hysteretic behavior due to the deep charge traps in the TiO<sub>2</sub> layer, related to the low electron mobility induced charge accumulation and UV light induced oxygen vacancies, [8-9] has prevented the correct evaluation of their device performance. As an alternative to the TiO<sub>2</sub> layers, organic materials have been used to fabricate the p-i-n type perovskite solar cells. Thus, solution-processable poly (3, 4-ethylenedioxythiophene):poly (styrenesulfonate) (PEDOT: PSS) and 6, 6-phenyl C<sub>61</sub>-butyric acid methyl ester (PCBM) [10-12] have been mainly adopted for a hole transport layer (HTL) and an ETL, respectively, which shows still lower efficiency than the n-i-p devices employing the TiO<sub>2</sub> ETL.

Fullerenes such as phenyl-C<sub>61</sub>-butyric acid methyl ester (PCBM) and C<sub>60</sub> [13-15] have been used as the ETL in perovskite solar cells because they are known to reduce the density of trap states and passivate the grain boundaries of methylammonium lead iodide (CH<sub>3</sub>NH<sub>3</sub>PbI<sub>3</sub>) absorbing layer [15-16]. In addition, the C<sub>60</sub> can be packed more densely than PCBM to facilitate intermolecular charge transport, and shows much higher electron mobility (1.6 cm<sup>2</sup>/V•s) and conductivity (2.3×10<sup>-3</sup> S/cm) compared to the PCBM (6.1×10<sup>-2</sup> cm<sup>2</sup>/V•s and 3.2 ×10<sup>-4</sup> S/cm, respectively) [17]. Thus, it is reported that the p-i-n type perovskite solar cells adopting the solution-processed C<sub>60</sub> layers showed better performance than the devices using PCBM and indene-C<sub>60</sub> bisadduct interface layers [17-19]. However, a very low solubility of C<sub>60</sub> in commonly used solvents makes it difficult to deposit a compact C<sub>60</sub> layer with complete coverage using the solution process [20]. Thus, it is highly required for a compact C<sub>60</sub> material for complete coverage placed on the bottom ETL in the n-i-p architecture. Also, the realization of n-i-p structure with low-temperature processing would make the device architecture much more favorable, due to versatile choices of p-type layers and effective realization of tandem perovskite structures [11,22]. In this regard, W. Ke et. al, [21] reported a planar

perovskite solar cell with 16% efficiency using a vacuum-processed C<sub>60</sub> ETL with a thickness of 7.5 nm. However, they showed a noticeable photocurrent hysteresis with relatively lower efficiency compared to the perovskite solar cell adopting the TiO<sub>2</sub> layer.

## **2.3 Electrodes for Flexible Perovskite Solar Cell**

### **2.3.1. Overview of Non-ITO Transparent Electrode**

With its superior electric and mechanical properties, graphene once was the rising star of the alternative electrodes. As soon as it was adopted in Perovskite Solar Cell, graphene proved its potential with cell performance equal to that of ITO. Various follow up studies showed mechanical advantages of graphene by applying graphene to flexible cells [23-24]. Despite these major studies, graphene was unable to come up with industrial examples since none of these studies have shown large area cells. In other words, no graphene electrode was able to overcome its physical defects that increased sheet resistance. Ag NW was also a well-known alternative transparent electrode for perovskite solar cell [25-27]. Due to its reactive characteristics, Ag NW was capable of forming AgI precipitation during perovskite deposition. Therefore, a firm passivation layer using solution process is required for Ag NW electrode, which limited its usage to certain materials.

The initial form of hybrid was simply stacking two promising

candidates. The simplest way to passivate Ag NW and enhance the conductivity of damaged graphene. Preliminary testing showed that a single layer of graphene is capable of Ag NW passivation as shown in figure 2.2. The Ag NW without graphene was oxidized and turned its color to yellow after 40 days in ambient condition. To precisely control the graphene transfer on Ag NW, the Ag NW was spin-coated on UVO treated glass substrate and covered with graphene by transfer process. The transfer process had various failure cases. For both wet and dry transfer process, graphene had PMMA as its supporting layer to keep its flatness during the process. PMMA is then removed with acetone and baked at high temperature (200°C) which caused Ag NW to melt and increase the resistance. The surface energy of Ag NW was not strong enough to strongly hold graphene layer from thermal release tape (TRT) during dry transfer and caused multiple defects on graphene layer, which then caused Ag NW oxidation after some period of time. Also, the graphene layer could not totally wrap around bumpy Ag NW. As a result, the initial trial of graphene Ag NW exposed multiple weaknesses. The suspended graphene left multiple vacancies under the suspended graphene layer which caused unwanted reaction with Ag NW as shown in figure 2.3(b). Also, the bumpy surface caused



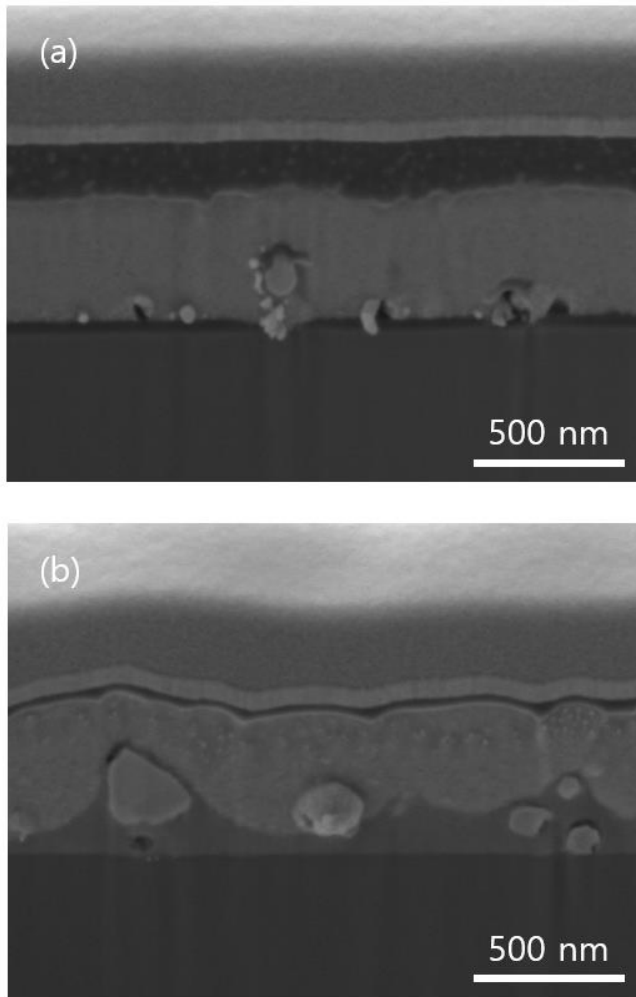


**Figure 2.3** The cross-sectional SEM image of (a) normal perovskite solar cell structure with evaporated  $C_{60}$  layer as ETL and (b) inverted perovskite solar cell structure with spin-coated PEDOT:PSS layer as HTL. Transporting layer with evaporation deposition method had discontinuity while that of spin-coating method had very poor uniformity.

### **2.3.2. Selecting Stable Polymer Substrate for Flexible Electrode.**

Through numerous examples, it is evitable that Ag NW required chemical passivation along with a method to maintain the flatness of the substrate surface. To do so, we came up with an idea to integrate graphene and Ag NW into a flat surface by using optically transparent polymer as its backbone as shown in figure 2.4. The polymer should be noble and chemically stable. Some of the well-known candidates are polydimethylsiloxane (PDMS), polyethylene naphthalate (PEN), polyethylene terephthalate (PET), polycarbonate (PC), and polyimide (PI). PE-group polymers are very stable and are used in various flexible devices as stable substrate. But it exists in solid phase only. Ag NW cannot be integrated nor embedded in PE- group materials. PDMS is liquid processable polymer widely used in biology and soft-lithography area. It is very stable and processable, but the material expands its volume in wet conditions such as DI bath during wet transfer. Polycarbonate is a transparent polymer that was used as backbone of Ag NW electrode for perovskite solar cell. It is solution processable, but is weak to certain organic solvents. Therefore, the whole fabrication process had to be limited. Past studies have adopted 2-step method,

vacuum evaporation and IPA based solution process, to fabricate perovskite layer without affecting the polymer layer. PI is well known polymer with good chemical resistance and thermal stability. It is solution processable and suites every criteria as a backbone polymer. But PI polymer is not colorless, it is not totally transparent. Fortunately, colorless polyimide does exist. Colorless PI (cPI) is a modified polyimide by elimination of Sulfur within its equation to have better transparency. Since polyimide has shown best results, cPI was applied as backbone polymer of Ag NW. Normal PI has shown firm chemical resistivity over organic solvents, but that of cPI did not. Chemical resistivity of cPI was further tested with other supplemental layer deposited on Ag NW embedded layer. cPI did react to organic solvents, like DMF and DMSO, and failed to keep sheet resistance low. Figure 2.5 graphically shows the variation of passivation layers stacked on cPI substrate for chemical stability test. Lastly, amorphous Teflon was tested as the backbone polymer. Teflon, also known as polytetrafluoroethylene, is commonly known for its low coefficients of friction and hydrophobicity. Teflon is normally not solution processable, but the modified amorphous Teflon is in liquid phase and can be applied to embed Ag NW. Amorphous Teflon was chemically and

thermally very stable and maintained the sheet resistance throughout. The transparency of amorphous Teflon was superb as well. The results for various polymer candidates are shown in table 2.1.

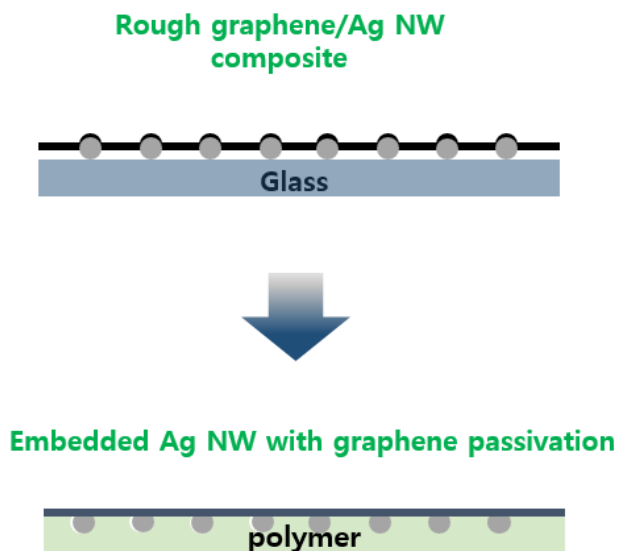


**Figure 2.4** Conceptual structure of graphene Ag NW composite on glass substrate and embedding in transparent polymer.

	chemical resistivity	compatibility	comment
PDMS	O	X	volume expansion
PEN	O	X	not processable
PET	O	X	not processable
PC	low	O	low chemical resistivity
PI	O	X	low transparency
cPI	low	O	spin-processable
AF Teflon	O	O	hydrophobic

**Table 2.1** List of transparent polymer candidate for Ag NW embedding. Each material was tested with organic solvent to compare its chemical resistivity toward perovskite fabrication.

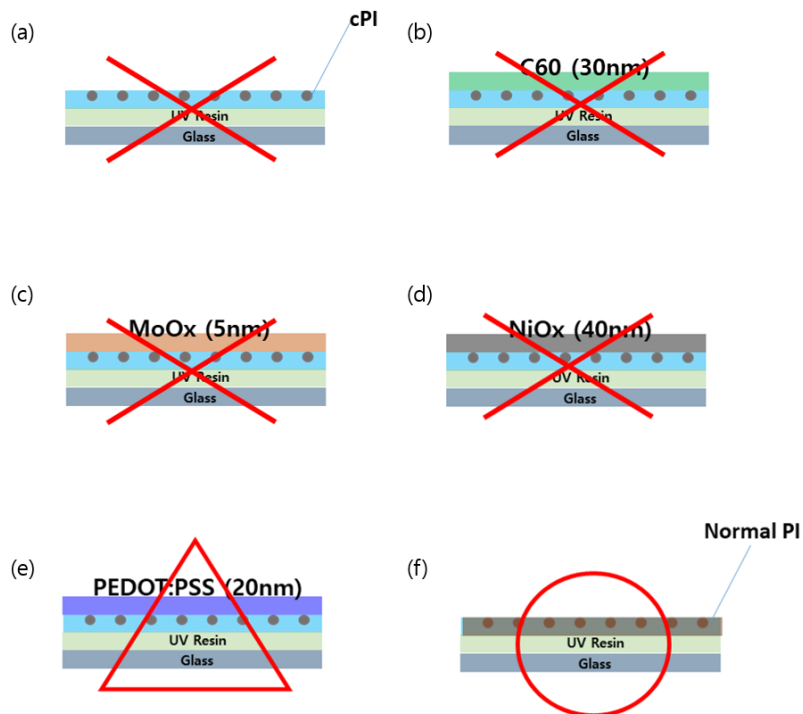


**Figure 2.5** Graphical results for cPI and PI chemical resistivity test. Each sample is tested with organic solvent such as DMF and DMSO. The result is shown with red marks: X and triangle indicate total and partial failure and O indicates success. The sample condition is listed as the following: (a) bare cPI, (b) cPI with evaporated C<sub>60</sub>, (c) cPI with evaporated molybden oxide, (d) cPI with spin-coated nickel oxide nanoparticle, (e) cPI with spin-coated PEDOT:PSS, and (f) normal PI layer as a reference sample.

## 2.4. References

- [1] Ball, J. M., Lee, M. M., Hey, A., & Snaith, H. J. (2013). Low-temperature processed meso-superstructured to thin-film perovskite solar cells. *Energy & Environmental Science*, 6(6), 1739-1743.
- [2] Heo, J. H., Im, S. H., Noh, J. H., Mandal, T. N., Lim, C. S., Chang, J. A., ... & Grätzel, M. (2013). Efficient inorganic–organic hybrid heterojunction solar cells containing perovskite compound and polymeric hole conductors. *Nature photonics*, 7(6), 486.
- [3] Eperon, G. E., Burlakov, V. M., Docampo, P., Goriely, A., & Snaith, H. J. (2014). Morphological control for high performance, solution-processed planar heterojunction perovskite solar cells. *Advanced Functional Materials*, 24(1), 151-157.
- [4] Park, N. G. (2013). Organometal perovskite light absorbers toward a 20% efficiency low-cost solid-state mesoscopic solar cell. *The Journal of Physical Chemistry Letters*, 4(15), 2423-2429.
- [5] Zhou, H., Chen, Q., Li, G., Luo, S., Song, T. B., Duan, H. S., ... & Yang, Y. (2014). Interface engineering of highly efficient perovskite solar cells. *Science*, 345(6196), 542-546.
- [6] Tao, C., Neutzner, S., Colella, L., Marras, S., Kandada, A. R. S., Gandini, M., ... & Bertarelli, C. (2015). 17.6% stabilized efficiency in low-temperature processed planar perovskite solar cells. *Energy & Environmental Science*, 8(8), 2365-2370.
- [7] Snaith, H. J., Abate, A., Ball, J. M., Eperon, G. E., Leijtens, T., Noel, N. K., ... & Zhang, W. (2014). Anomalous hysteresis in perovskite solar cells. *J. Phys. Chem. Lett*, 5(9), 1511-1515.

- [8] Unger, E. L., Hoke, E. T., Bailie, C. D., Nguyen, W. H., Bowring, A. R., Heumüller, T., ... & McGehee, M. D. (2014). Hysteresis and transient behavior in current–voltage measurements of hybrid-perovskite absorber solar cells. *Energy & Environmental Science*, 7(11), 3690-3698.
- [9] Li, Y., Zhao, Y., Chen, Q., Yang, Y., Liu, Y., Hong, Z., ... & Yang, Y. (2015). Multifunctional fullerene derivative for interface engineering in perovskite solar cells. *Journal of the American Chemical Society*, 137(49), 15540-15547.
- [10] Docampo, P., Ball, J. M., Darwich, M., Eperon, G. E., & Snaith, H. J. (2013). Efficient organometal trihalide perovskite planar-heterojunction solar cells on flexible polymer substrates. *Nature communications*, 4, 2761.
- [11] Seo, J., Park, S., Kim, Y. C., Jeon, N. J., Noh, J. H., Yoon, S. C., & Seok, S. I. (2014). Benefits of very thin PCBM and LiF layers for solution-processed p–i–n perovskite solar cells. *Energy & Environmental Science*, 7(8), 2642-2646.
- [12] You, J., Hong, Z., Yang, Y., Chen, Q., Cai, M., Song, T. B., ... & Yang, Y. (2014). Low-temperature solution-processed perovskite solar cells with high efficiency and flexibility. *ACS nano*, 8(2), 1674-1680.
- [13] Heo, J. H., Han, H. J., Kim, D., Ahn, T. K., & Im, S. H. (2015). Hysteresis-less inverted CH<sub>3</sub>NH<sub>3</sub>PbI<sub>3</sub> planar perovskite hybrid solar cells with 18.1% power conversion efficiency. *Energy & Environmental Science*, 8(5), 1602-1608.

- [14] Liu, Y., Bag, M., Renna, L. A., Page, Z. A., Kim, P., Emrick, T., ... & Russell, T. P. (2016). Understanding interface engineering for high-performance fullerene/perovskite planar heterojunction solar cells. *Advanced Energy Materials*, 6(2), 1501606.
- [15] Shao, Y., Xiao, Z., Bi, C., Yuan, Y., & Huang, J. (2014). Origin and elimination of photocurrent hysteresis by fullerene passivation in CH<sub>3</sub>NH<sub>3</sub>PbI<sub>3</sub> planar heterojunction solar cells. *Nature communications*, 5, 5784.
- [16] Abrusci, A., Stranks, S. D., Docampo, P., Yip, H. L., Jen, A. K. Y., & Snaith, H. J. (2013). High-performance perovskite-polymer hybrid solar cells via electronic coupling with fullerene monolayers. *Nano letters*, 13(7), 3124-3128.
- [17] Liang, P. W., Chueh, C. C., Williams, S. T., & Jen, A. K. Y. (2015). Roles of fullerene-based interlayers in enhancing the performance of organometal perovskite thin-film solar cells. *Advanced Energy Materials*, 5(10), 1402321.
- [18] Bi, C., Yuan, Y., Fang, Y., & Huang, J. (2015). Low-Temperature Fabrication of Efficient Wide-Bandgap Organolead Trihalide Perovskite Solar Cells. *Advanced Energy Materials*, 5(6), 1401616.
- [19] Li, Y., Ye, S., Sun, W., Yan, W., Li, Y., Bian, Z., ... & Huang, C. (2015). Hole-conductor-free planar perovskite solar cells with 16.0% efficiency. *Journal of Materials Chemistry A*, 3(36), 18389-18394.
- [20] Wojciechowski, K., Leijtens, T., Siprova, S., Schlueter, C., Hörantner, M. T., Wang, J. T. W., ... & Snaith, H. J. (2015). C60 as an efficient n-type compact layer in perovskite solar cells. *The journal of physical chemistry letters*, 6(12), 2399-2405.

- [21] Ke, W., Zhao, D., Grice, C. R., Cimaroli, A. J., Ge, J., Tao, H., ... & Yan, Y. (2015). Efficient planar perovskite solar cells using room-temperature vacuum-processed C 60 electron selective layers. *Journal of Materials Chemistry A*, 3(35), 17971-17976.
- [22] Jung, H. S., & Park, N. G. (2015). Perovskite solar cells: from materials to devices. *small*, 11(1), 10-25.
- [23] Sung, H., Ahn, N., Jang, M. S., Lee, J. K., Yoon, H., Park, N. G., & Choi, M. (2016). Transparent Conductive Oxide-Free Graphene-Based Perovskite Solar Cells with over 17% Efficiency. *Advanced Energy Materials*, 6(3), 1501873.
- [24] Yoon, J., Sung, H., Lee, G., Cho, W., Ahn, N., Jung, H. S., & Choi, M. (2017). Superflexible, high-efficiency perovskite solar cells utilizing graphene electrodes: towards future foldable power sources. *Energy & Environmental Science*, 10(1), 337-345.
- [25] Li, Y., Meng, L., Yang, Y. M., Xu, G., Hong, Z., Chen, Q., ... & Li, Y. (2016). High-efficiency robust perovskite solar cells on ultrathin flexible substrates. *Nature communications*, 7, 10214.
- [26] Kim, K., Kwon, H. C., Ma, S., Lee, E., Yun, S. C., Jang, G., ... & Moon, J. (2018). All-Solution-Processed Thermally and Chemically Stable Copper–Nickel Core–Shell Nanowire-Based Composite Window Electrodes for Perovskite Solar Cells. *ACS applied materials & interfaces*, 10(36), 30337-30347.
- [27] Dong, H., Wu, Z., Jiang, Y., Liu, W., Li, X., Jiao, B., ... & Hou, X. (2016). A flexible and thin graphene/silver nanowires/polymer hybrid transparent electrode for optoelectronic devices. *ACS applied materials & interfaces*, 8(45), 31212-31221.

## Chapter 3.

# Hysteresis-free Flexible Perovskite Solar Cells by Utilizing C<sub>60</sub> as Electron Transporting Layer

---

### 3.1. Introduction

Hysteresis-free, highly efficient and stable perovskite solar cells processed at low temperatures are strongly demanded to realize flexible or perovskite-based tandem solar cells. Here, we report a hysteresis-free planar CH<sub>3</sub>NH<sub>3</sub>PbI<sub>3</sub> perovskite solar cell with a power conversion efficiency of 19.1% using a room-temperature vacuum-processed C<sub>60</sub> electron transport layer (ETL) without the hole blocking layer. By optimizing the thickness of C<sub>60</sub> layer, the highly homogeneous, uniform, and dense ETL with a thickness of 35 nm is found to not only passivate the grain boundaries and surfaces of the perovskite layer, but also enhance charge transport property. Thus, the C<sub>60</sub> layer deposited on

perovskites eliminates the photocurrent hysteresis and improves the cell efficiency. Also, compared to the device adopting the C<sub>60</sub> and bathocuproine (BCP) combination, the one with the C<sub>60</sub> layer without BCP layer shows better performance due to enhanced electron extraction property. Furthermore, for the first time, we demonstrate a hysteresis-free flexible perovskite solar cell using the C<sub>60</sub> ETL on polyethylene naphthalate (PEN) substrate with 16.0% efficiency.

Organic/inorganic hybrid perovskites have been considered promising materials to use in the photoactive layers of solar cells due to their superb power conversion efficiency (PCE) and simple processes along with low material costs [1-4]. Also, the rapid energy payback time of perovskite solar cells was recently demonstrated as a key advantage by an environmental examination using life cycle assessment [5]. Their high absorption coefficient, balanced electron/hole mobility, smaller exciton binding energy, and longer exciton diffusion length than those of organic materials [6-10] enable researchers to continuously increase the device efficiencies from 3.8% in 2009 to 22.1% in 2016 [3,11,12]. The perovskite solar cells with high performances have usually adopted the n-i-p architecture, commonly using TiO<sub>2</sub> material as an electron transport layer (ETL) [13-16]. Here the TiO<sub>2</sub>

compact layer requires a high-temperature process over 450 °C, which precludes its application on flexible substrates. To solve this limitation, low-temperature solution-processed TiO<sub>2</sub> has been used as the ETL [17-19]. However, the serious hysteretic behavior due to the deep charge traps in the TiO<sub>2</sub> layer, related to the low electron mobility induced charge accumulation and UV light induced oxygen vacancies, [20,21] has prevented the correct evaluation of their device performance. As an alternative to the TiO<sub>2</sub> layers, organic materials have been used to fabricate the p-i-n type perovskite solar cells. Thus, solution-processable poly (3, 4-ethylenedioxythiophene):poly (styrenesulfonate) (PEDOT: PSS) and 6, 6-phenyl C<sub>61</sub>-butyric acid methyl ester (PCBM) [22-24] have been mainly adopted for a hole transport layer (HTL) and an ETL, respectively, which shows still lower efficiency than the n-i-p devices employing the TiO<sub>2</sub> ETL.

Fullerenes such as phenyl-C<sub>61</sub>-butyric acid methyl ester (PCBM) and C<sub>60</sub> [25-27] have been used as the ETL in perovskite solar cells because they are known to reduce the density of trap states and passivate the grain boundaries of methylammonium lead iodide (CH<sub>3</sub>NH<sub>3</sub>PbI<sub>3</sub>) absorbing layer [27,28]. In addition, the C<sub>60</sub> can be packed more densely than PCBM to facilitate intermolecular charge transport, and

shows much higher electron mobility ( $1.6 \text{ cm}^2/\text{V}\cdot\text{s}$ ) and conductivity ( $2.3 \times 10^{-3} \text{ S/cm}$ ) compared to the PCBM ( $6.1 \times 10^{-2} \text{ cm}^2/\text{V}\cdot\text{s}$  and  $3.2 \times 10^{-4} \text{ S/cm}$ , respectively) [29]. Thus, it is reported that the p-i-n type perovskite solar cells adopting the solution-processed  $\text{C}_{60}$  layers showed better performance than the devices using PCBM and indene- $\text{C}_{60}$  bisadduct interface layers [29-31]. However, a very low solubility of  $\text{C}_{60}$  in commonly used solvents makes it difficult to deposit a compact  $\text{C}_{60}$  layer with complete coverage using the solution process [32]. Thus, it is highly required for a compact  $\text{C}_{60}$  material for complete coverage placed on the bottom ETL in the n-i-p architecture. Also, the realization of n-i-p structure with low-temperature processing would make the device architecture much more favorable, due to versatile choices of p-type layers and effective realization of tandem perovskite structures [4,23]. In this regard, W. Ke et. al, [33] reported a planar perovskite solar cell with 16% efficiency using a vacuum-processed  $\text{C}_{60}$  ETL with a thickness of 7.5 nm. However, they showed a noticeable photocurrent hysteresis with relatively lower efficiency compared to the perovskite solar cell adopting the  $\text{TiO}_2$  layer. Furthermore, there have been no reports on a hysteresis-free flexible perovskite solar cell with high efficiency over 16 %.

Therefore, we aim to develop hysteresis-free high efficiency solar cell with low temperature process, and, here we demonstrate hysteresis-free n-i-p type perovskite solar cells with 19.1% efficiency comprising indium–tin oxide (ITO)/C<sub>60</sub>/CH<sub>3</sub>NH<sub>3</sub>PbI<sub>3</sub> (MAPbI<sub>3</sub>)/2,2', 7,7'-Tetrakis(N,N-di-p-methoxyphenylamino)-9,9'-spirobifluorene (spiro-MeOTAD)/Au. By controlling the thickness of C<sub>60</sub> layer, we found that a 35 nm-thick C<sub>60</sub> layer coated on the ITO electrode show homogenously compact structures with improved electron extraction, resulting in eliminating photocurrent hysteresis and showing the best efficiency of 19.1%. By comparing with the device adopting C<sub>60</sub> and BCP as the ETL and the hole blocking layer (HBL), respectively, the one with C<sub>60</sub> layer without HBL significantly improves the hysteresis and enhances the device performance due to better electron extraction property. The observed results was confirmed by impedance analysis, measured absorption spectra, and shunt/series resistance characterization. Moreover, we firstly demonstrate hysteresis-free flexible perovskite solar cells with over 16.0% efficiency by adopting the same n-i-p architecture.

## 3.2. Experimental Methods

### 3.2.1. Fabrication of Perovskite Solar Cells

The commercially purchased ITO (150-nm-thick)-coated glass substrate (AMG,  $9.5 \Omega \text{ cm}^2$ ,  $25 \times 25 \text{ mm}^2$ ) was used after sequential cleaning using UVO treatment for 30 min and ultrasonic method with acetone, isopropanol, and DI water for 15 min, respectively. After drying with nitrogen gas, the ITO glass substrate was exposed to UVO treatment in order to improve the surface energy. Compact and ultrathin layers of both BCP and  $\text{C}_{60}$  films were thermally deposited on the ITO glass substrate by thermal evaporator in a vacuum condition under  $< 10^{-7}$  Torr. The deposition rate and thickness of the organic layers were controlled by a quartz crystal sensor during the thermal evaporation process.

The perovskite active layer ( $\text{CH}_3\text{NH}_3\text{PbI}_3$ ,  $\text{MAPbI}_3$ ) with a thickness of 400 nm was fabricated on the  $\text{C}_{60}$  layer by using Lewis base adduct method.<sup>1</sup> To prepare a  $\text{CH}_3\text{NH}_3\text{I} \cdot \text{PbI}_2 \cdot \text{DMSO}$  (molar ratio 1:1:1) adduct solution, 159 mg of home-made methylammonium iodide ( $\text{CH}_3\text{NH}_3\text{I}$ ),<sup>2</sup> 461 mg of  $\text{PbI}_2$  (Sigma-Aldrich, 99 %), and 78 mg of *N,N*-dimethyl sulfoxide (DMSO, Sigma Aldrich, 99 %) were dissolved

in 600 mg of N,N-dimethylformamide (DMF, Sigma Aldrich, 99.8%) solution in a vacuum condition without heating. The prepared solution was deposited by spin-coating on the C<sub>60</sub> layer at 4000 rpm for 20 s with 0.5 ml of diethyl ether dripping method during the process, which causes rapid vaporization of DMF. After that, the perovskite coated substrate was annealed sequentially at 65 °C for 1 min and 100 °C for 2 min to make uniform and dense MAPbI<sub>3</sub> layer. Subsequently, spiro-MeOTAD layer with a thickness of 200 nm as hole transport material was fabricated on the perovskite active layer by spin-coating of 15- $\mu$ L spiro-MeOTAD solution at 3000 rpm for 25 s. The spiro-MeOTAD solution was synthesized using 72.3 mg of spiro-MeOTAD (Merck) in 1 mL chlorobenzene, 28.8  $\mu$ L of 4-tertbutyl pyridine (Sigma Aldrich) and 17.5  $\mu$ L of lithium bis(trifluoromethanesulfonyl) imide (Li-TSFI) solution of 520 mg in 1 ml acetonitrile (Sigma Aldrich). Finally, gold (Au) with a thickness of 50 nm was deposited as the counter electrode using thermal evaporator in a vacuum condition on the top of the HTM. Here the shadow mask with an area of 6.76 mm<sup>2</sup> was used to create the devices with an active area of 9 mm<sup>2</sup>.

Flexible perovskite solar cells comprised of PEN/ITO/C<sub>60</sub>/MAPbI<sub>3</sub>/HTM/Au structures were also fabricated to

demonstrate hysteresis-free perovskite-based flexible devices. The C<sub>60</sub> layer was deposited on the ITO-coated polyethylene-naphthalate (PEN, AMG Korea Inc.) substrate by thermal evaporation. Other layers were sequentially deposited by using the same procedure described above.

### 3.2.2. Characterization

The surface morphologies of the fabricated perovskite solar cells were detected by FE-SEM (AURIGA, Carl Zeiss). The cross-sectional images of the devices were examined by focused-ion-beam assisted SEM (FIB-SEM, AURIGA, Carl Zeiss). The transmittance of the substrate with/without the C<sub>60</sub> layer was investigated by UV/Vis spectrometer (Cary 5000, Agilent technologies) in the visible range from 300 to 800 nm. J-V characteristics of the fabricated perovskite solar cells were measured with a computer-controlled Keithley 2400 source meter at room temperature inside the glove box. The simulated AM 1.5G one sun illumination was provided by AAA class Newport solar simulator (Oriel Sol 3A) with 6279NS 450 W Xenon lamp. The light intensity of the solar simulator was calibrated to give 100 mWcm<sup>-2</sup> using a standard Si photovoltaic cell (RC-1000-TC-KG5-N, VLSI Standards). The hysteresis of the devices was investigated by measuring the forward and reverse scans of J-V curves at various scan rates from 20 to 800 ms at 20 mV per step. The external quantum efficiency (EQE) of the same devices used for J-V measurements was obtained from IPCE system (PV measurement Inc.) under DC mode

with a 75 W Xenon lamp (USHIO, Japan) as a light source.

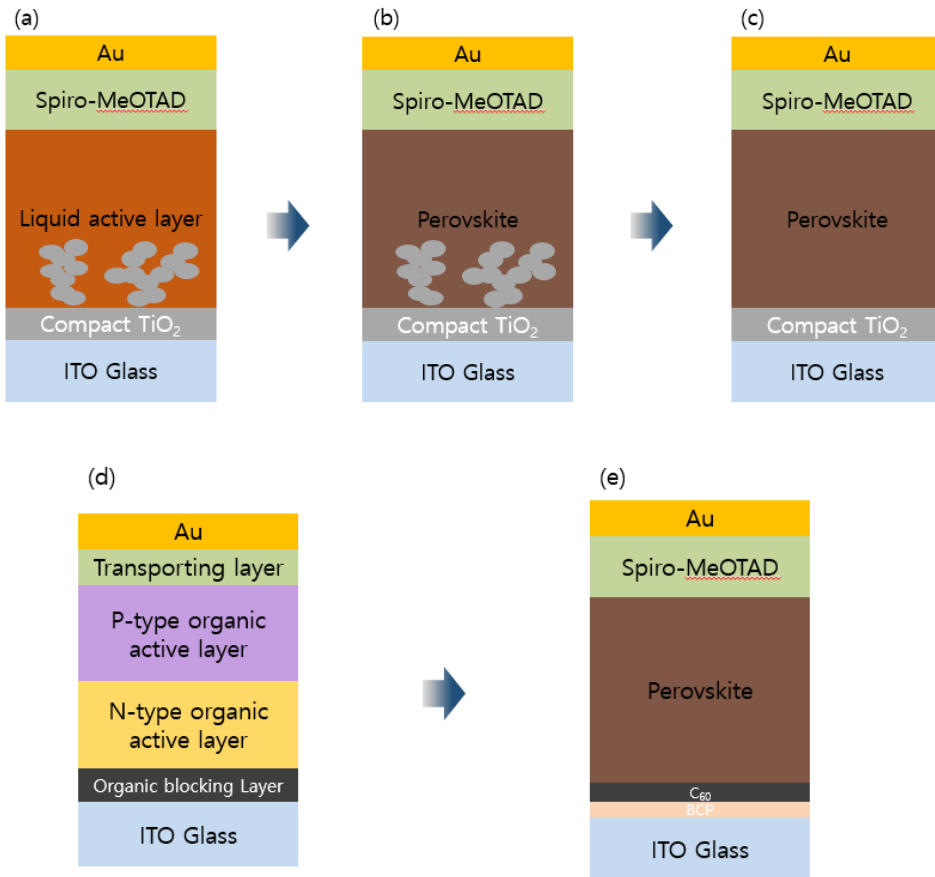
### 3.3. Results and Discussion

#### 3.3.1. Structure of C<sub>60</sub>-based Flexible Perovskite Solar Cell

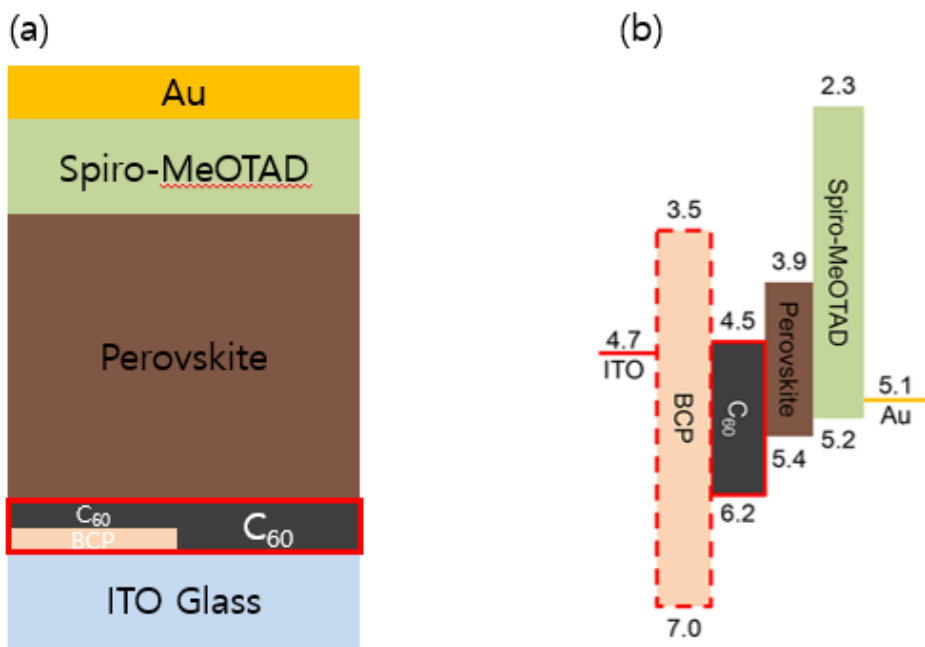
The structure of the C<sub>60</sub>-based flexible perovskite solar cell is schematically illustrated in figure 3.2. We adopted a normal perovskite solar cell structure using MAPbI<sub>3</sub> as absorbing layer. Spiro-MeOTAD and C<sub>60</sub> were used as HTL and ETL, respectively.

Figure 3.1 shows the evolution of conventional device configuration from perovskite solar cell consisting of Au/Spiro-MeOTAD/MAPbI<sub>3</sub>/mesoporous-TiO<sub>2</sub>/compact-TiO<sub>2</sub>/fluorine doped tin oxide (FTO) /Glass that produces the highest performance with hysteresis to our final perovskite solar cell consisting of Au/Spiro-MeOTAD/MAPbI<sub>3</sub>/C<sub>60</sub>/Indium tin oxide (ITO)/Glass. Past studies have shown perovskite solar cell structure without mesoporous TiO<sub>2</sub> layer, which required high temperature process. But the remaining TiO<sub>2</sub> compact layer still caused hysteresis and could not perform well. To develop hysteresis-free low temperature processed high efficiency solar cell that can be applied to flexible substrates, we fabricated planar

perovskite solar cells by replacing the TiO<sub>2</sub> layers with the C<sub>60</sub> layer as an ETL without the HBL such as BCP figure 3.2. Here, since we did not need a high-temperature process for mp-TiO<sub>2</sub> formation, ITO electrode with higher transmittance in a visible range than FTO electrode was utilized as a cathode on a glass substrate. Then, the C<sub>60</sub> layer was prepared by thermal evaporation in a vacuum environment on the ITO/glass substrate. Subsequently, the metal halide perovskite (MAPbI<sub>3</sub>) and Spiro-MeOTAD were spin coated on the top of C<sub>60</sub> layer. Finally, Au as an anode was thermally evaporated in a vacuum environment. Details of fabrication processes are described in the experimental section.



**Figure 3.1** The progress of perovskite solar cell structure from (a-c) DSSC and from (d-e) OPV to utilize flexible substrate.



**Figure 3.2** (a) the structure of perovskite solar cell and (b) the relative energy level diagram of the MAPbI<sub>3</sub> perovskite solar cell adapting C<sub>60</sub> as ETL with or without BCP layer. Red marks on both images indicate the BCP elimination.

### 3.3.2. Elimination of BCP Hole Blocking Layer

The energy band diagram of the MAPbI<sub>3</sub> based perovskite solar cells employing the C<sub>60</sub> layer as an ETL is represented in figure 3.2, where the HOMO and LUMO levels of BCP layer as a HBL are additionally drawn for comparison. In case of the BCP/C<sub>60</sub> layers commonly used as an ETL combination in a normal structure of organic photovoltaics (OPVs) [33-36], which is the same as the inverted structure (p-i-n) of perovskite solar cell, the BCP layer transports electrons through tunneling and partially prevents electron transport due to its lower LUMO level than the C<sub>60</sub> and MAPbI<sub>3</sub> layers, while its higher HOMO level blocks effectively hole transport. Even with dropping the HBL, we can expect that the continuous energy levels between the electrodes and the perovskite layer allow efficient electron/hole transport along with low leakage loss.

To compare the performance of MAPbI<sub>3</sub> based devices adopting C<sub>60</sub> layer with the ones incorporating C<sub>60</sub>/BCP layer, we measured device characteristics with varying the thicknesses of BCP from 0 nm to 20 nm under air mass 1.5 global (AM 1.5G) conditions. Figure 3.3 shows representative (J-V) characteristics of the MAPbI<sub>3</sub> solar cells employing

a 35-nm-thick  $C_{60}$  layer with or without BCP layer. As we increase the thickness of BCP layer, the device shows degraded performance, and the photocurrent hysteresis is significantly increased. It is noted that the BCP layer, a well-known effective HBL in OPVs [34,37], is only effective with a maximum thickness of 10 nm due to its low mobility and limited electron transporting rate through tunneling effect. To investigate the difference in J-V characteristics between the  $C_{60}$  based device and the  $C_{60}$ /BCP based ones, electrochemical impedance spectroscopy (EIS) analysis was performed under illumination condition, applying a 25 mV AC signal over the constant applied bias of 1.05 V in the frequency range from 0.1 kHz to 50 MHz. Nyquist plot of the device with  $C_{60}$  or  $C_{60}$ /BCP as shown in figure 3.3 exhibits a semicircle in a relatively high frequency range ( $> 1$  kHz), implying that the total series resistance is mainly influenced by the interfacial charge-transfer resistance [38]. The smaller semicircle corresponding to the  $C_{60}$  based device than that of  $C_{60}$ /BCP based devices indicates a lower charge transfer resistance in the interface between the ITO electrode and the  $C_{60}$ /perovskite layers. Also, it is found that the little humps in a semicircle at a high frequency regime are observed only for the devices with  $C_{60}$ /BCP, indicating the additional Resistor Capacitor (RC)

component due to the BCP layer adversely affects the transport property. Also, the  $R_s$  estimated from the leftmost end of the semicircle at a high frequency limit increases as the thickness of BCP layer increases, which coincides well with the measured series resistance ( $R_s$ ) values from the J-V characteristic as shown in figure 3.3. These observed results support the higher Fill Factor (FF) of the device adopting the  $C_{60}$  layer compared to the device with the  $C_{60}/BCP$  combination. Thus, by taking out the BCP layer, the device not only shows increased overall performance, but also reveals hysteresis-free characteristics with negligible 0.005% difference between the forward scan and the backward scan. This suggests that the existence of BCP layer does not give any positive effects toward overall efficiency of the  $MAPbI_3$  based perovskite solar cells; rather it could cause unnecessary trap states that leads to hysteresis loss.

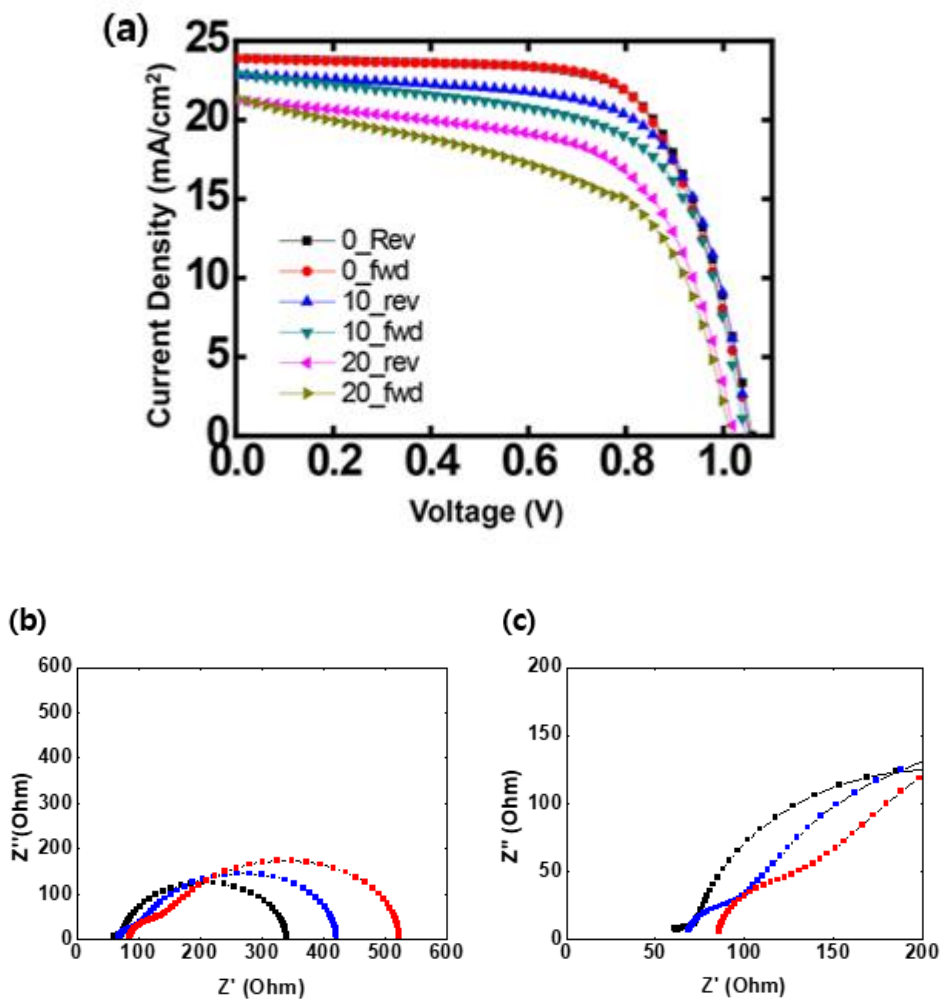


**Figure 3.3** (a) J-V curves of the devices adapting C<sub>60</sub> layer with and without BCP layer (b,c) The Nyquist plots of planar heterojunction perovskite solar cells adapting C<sub>60</sub> layer with and without BCP layer

### 3.3.3. C<sub>60</sub> Optimization

To identify the optimum thickness of C<sub>60</sub> as an ETL in MAPbI<sub>3</sub> solar cells, systematic characterization of the C<sub>60</sub> based device was performed because the C<sub>60</sub> layer was used as an effective light absorbing layer in planar OPVs with a band gap energy of 1.7 eV [34-36]. Figure 3.6 shows the main figure of merit of the measured samples, i.e., short-circuit current density ( $J_{sc}$ ), open-circuit voltage ( $V_{oc}$ ), FF, PCE, shunt resistance, and series resistance depending on the different thickness of C<sub>60</sub> layer. As the thickness increases up to 40 nm, the transmittance of the C<sub>60</sub>/ITO/Glass is gradually decreased while noticeable reduction in transmittance in a wavelength of 350 nm to 550 nm is appeared as shown in figure 3.4. Thus, it is reasonable to observe a little drop in  $J_{sc}$  due to the decreased absorption in the perovskite layer. However, the  $V_{oc}$  starts to increase and reaches the peak value at 35 nm, while  $J_{sc}$  shows little variations. These results indicate that as the thickness increases, the C<sub>60</sub> layer itself absorbs incident light as an active layer and creates excitons in this layer. Then, the generated electrons and holes in the LUMO and HOMO levels of

$C_{60}$  layer are efficiently separated and moved toward the ITO electrode and the perovskite layer, respectively, resulting in improved carrier transport in the device. This explanation can be verified by the measured  $R_S$  and shunt resistance ( $R_{SH}$ ) as shown in figure 3.6; as the thickness of  $C_{60}$  increases, the  $R_S$  continuously drops to a thickness of 35 nm and then goes up at 40 nm thickness while the  $R_{SH}$  increases to 30 nm and then saturates at a thickness thicker than 30 nm. However, the conductivity of  $C_{60}$  layer does limits the maximum thickness, which can be confirmed by the increased  $R_S$  as the thickness exceeds a thickness of 40 nm as shown in figure 3.6. Also, the cross-sectional SEM images of the devices with the different thickness of  $C_{60}$  layer (figure 3.5) show that the  $C_{60}$  layer with a thickness below 30 nm has lots of pin-holes that can connect the ITO electrode directly with the perovskite layer. Thus, the  $C_{60}$  layer with more than a 30-nm-thick is needed to fully and uniformly cover the underlying ITO electrode, which can improve the electron transport property and reduce the leakage loss at the interface. the perovskite active layer due to increased absorption in the  $C_{60}$  layer, but does highly enhance the carrier transport

consequently leading to the improvement in overall device performances.

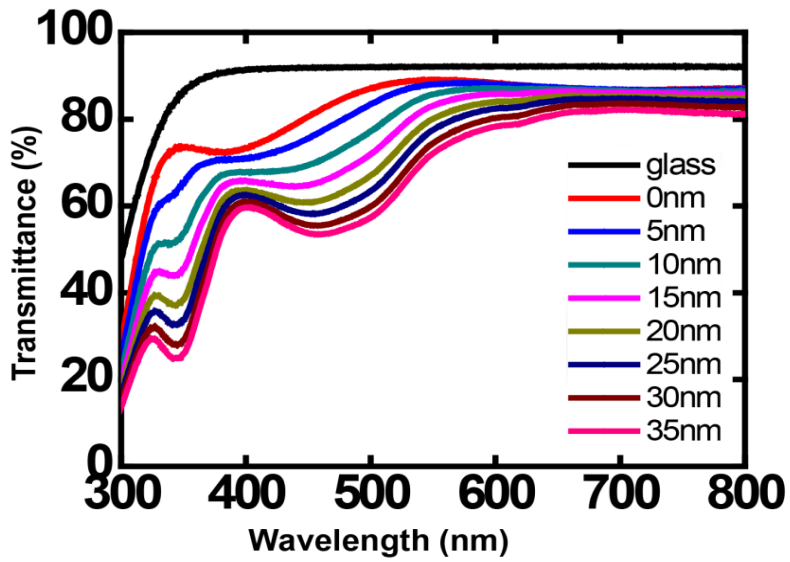


**Figure 3.4** Variation in the transmittance of C<sub>60</sub>/ITO/Glass with different thickness of C<sub>60</sub> layer from 0 nm to 35 nm.

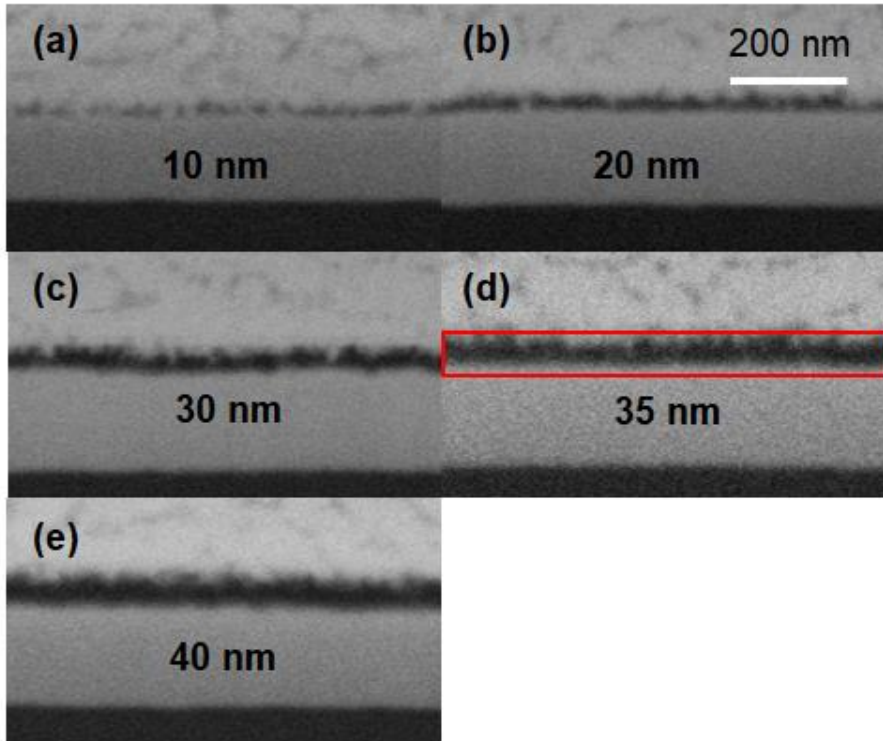


**Figure 3.5** (a-e) Cross-sectional SEM images of the devices with different C<sub>60</sub> thickness. Minimum thickness of 30 nm is required for C<sub>60</sub> deposition to have a uniform layer that covers the surface. Optimum thickness is 35 nm with best performance.

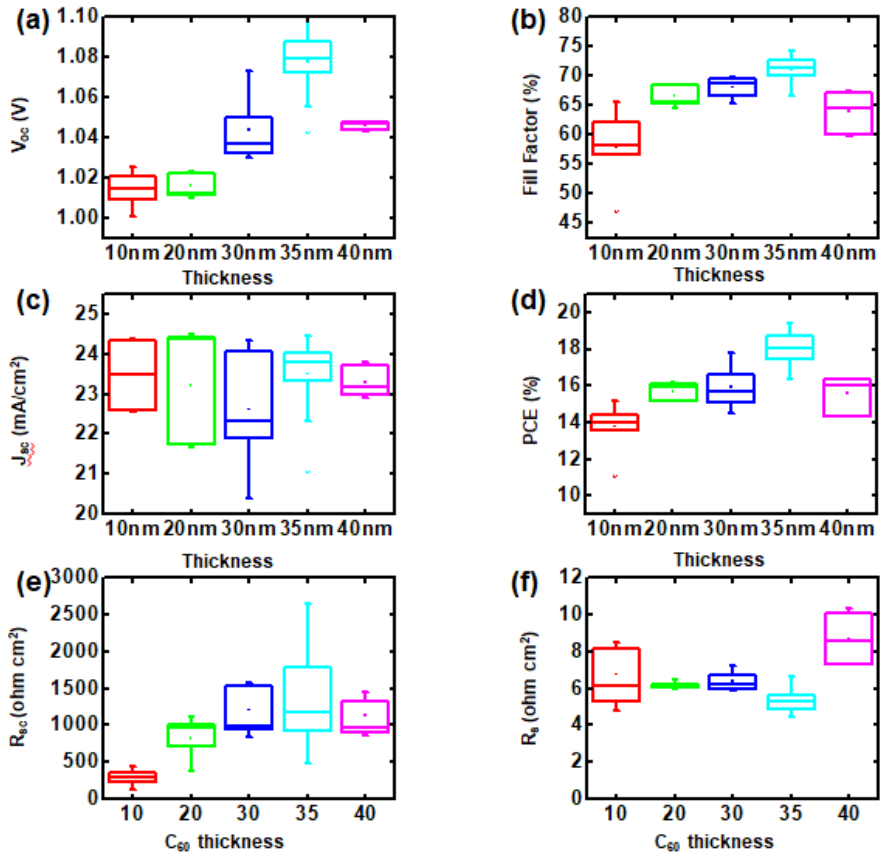


**Figure 3.6** (a) Open circuit voltage ( $V_{oc}$ ), (b) fill factor, (c) current density ( $J_{sc}$ ), (d) PCE, (e) shunt resistance, and (f) series resistance comparison with different  $C_{60}$  thickness.

### 3.3.4. Performance of the Perovskite Solar Cell

Figure 3.7 show current density versus voltage (J-V) curve and external quantum efficiency (EQE) data of the best performance cell, respectively. This cell was measured with various dwelling time from 20 ms to 800 ms at mV per step depending on the voltage scan direction in order to confirm that there is no photocurrent hysteresis. The integrated photocurrent from the EQE spectrum was calculated as 23.3 mA/cm<sup>2</sup>, which is close to the  $J_{sc}$  obtained from J-V measurements. Table 3.1 summarizes the device parameters for the best cell, showing less than 0.002% difference between the forward scan and the backward scan. Table 3.1 and represents the averages and standard deviation values of the photovoltaic parameters obtained for 92 planar cells. To perform stability analysis for the best cell, we took a steady-state photocurrent output for 10 minutes at a bias of 0.82 V, which corresponds to the maximum power point, as shown in figure 3.8. The cell yielded a stabilized current density of 21.7 mA/cm<sup>2</sup>, corresponding to a power output of 17.8 mW/cm<sup>2</sup>. Therefore, by applying the C<sub>60</sub> layer with an optimized thickness of 35 nm to the planar-type perovskite solar cell as an ETL, we were able to firstly

develop hysteresis-free low-temperature-processed cell with the best PCE of 19.1%. The corresponding EQE data of the MAPbI<sub>3</sub> based perovskite solar cell also shows high values of approximately 90% in the visible range except some decrease in a wavelength of 350 nm to 500 nm due to the slight light absorption by the C<sub>60</sub> layer as shown in figure 3.7.

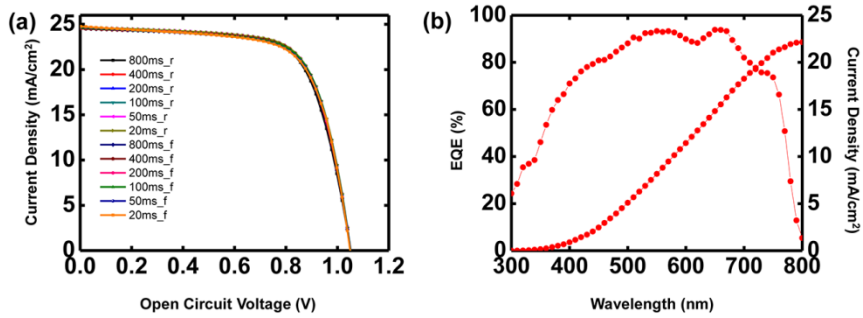


**Figure 3.7** (a) J-V characteristics of the MAPbI<sub>3</sub> perovskite cells measured at forward scan and reverse scan with various dwelling time (20 ms to 800 ms) at 20 mV per step (b) EQE profile and integrated photocurrent density of the best performing device.

	$V_{oc}$ (V)	$J_{sc}$ (mA/cm <sup>2</sup> )	Fill Factor (%)	PCE (%)
<b>Planar cell</b>	<b>1.07 ± 0.02</b>	<b>22.11 ± 0.78</b>	<b>70.43 ± 2.29</b>	<b>17.85 ± 0.83</b>

**Table 3.1** Statistical results of the performance of the perovskite solar cells on glass/ITO substrate employing C<sub>60</sub> electron transporting layer.

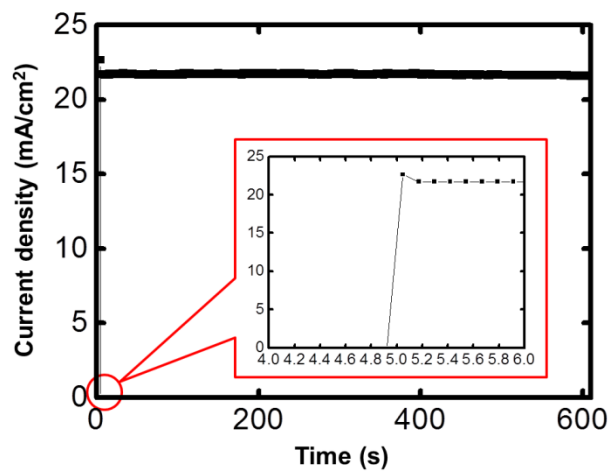


**Figure 3.8** Steady-state photocurrent measurement of the fabricated planar perovskite solar cell for 10 min at 0.82 V, which corresponds to the maximum power point. The inset shows current response of devices switched from open-circuit to short-circuit under illumination.

### 3.3.5. Performance of Flexible Perovskite Solar Cells

To verify that our strategy is applicable to flexible solar cells, we fabricated the MAPbI<sub>3</sub> based perovskite solar cell with the C<sub>60</sub> ETL on ITO-coated polyethylene naphthalate (PEN) substrates as schematically shown in figure 3.10. By investigating the cross-sectional view of the device structure with field emission scanning electron microscope (FE-SEM) (figure 3.10b), we confirmed that the C<sub>60</sub> layer with a thickness of 35 nm is uniformly and densely coated on the underlying ITO/PEN substrate and well separates the ITO electrode from the perovskite active layer. Then, we were firstly able to demonstrate a flexible, hysteresis-free perovskite solar cell with the highest efficiency of 16.0%, which is the highest one among flexible CH<sub>3</sub>NH<sub>3</sub>PbI<sub>3</sub> solar cells (figure 3.10c). Here, the inset shows the digital camera image of the fabricated flexible perovskite solar cell. The measured device parameters of the best cell depending on the direction of voltage scan rate are summarized at table 3.2 in order to show no appreciable change in  $J_{SC}$ ,  $V_{OC}$ ,  $FF$ , and PCE. Also, the average values with standard deviations of the device parameters for 44 flexible cells are shown in table 3.2. To observe the device stability against mechanical bending of

the flexible cells, we performed a bending test during 1000 consecutive bending cycles at different radii of curvatures ( $R_b$ ) of 10 mm and 5 mm. The flexible cells at  $R_b$  of 10 mm exhibited no appreciable decrease in PCE, retaining its initial PCE as shown in figure 3.10d. Meanwhile, the flexible cells at  $R_b$  of 5 mm showed 95% of initial PCE after 100 bending cycles, and the PCE decreased by approximately 20 % compared with the initial efficiency after 1000 cycles (figure 3.10d). Thus, the observed results demonstrate that these flexible cells have good device stability against the mechanical bending, which agrees well with the previous report adopting ITO electrode [39]. Here, a little lower efficiency of the flexible cell than that of the cell on a glass substrate is mainly attributed to the use of a rigid ITO electrode, which becomes brittle after cyclic bending. By replacing this brittle ITO electrode with the one suitable for flexible substrates, we will be able to increase the cell efficiency and stability comparable to the cell on a glass substrate, which is on-going research from several research groups including us.

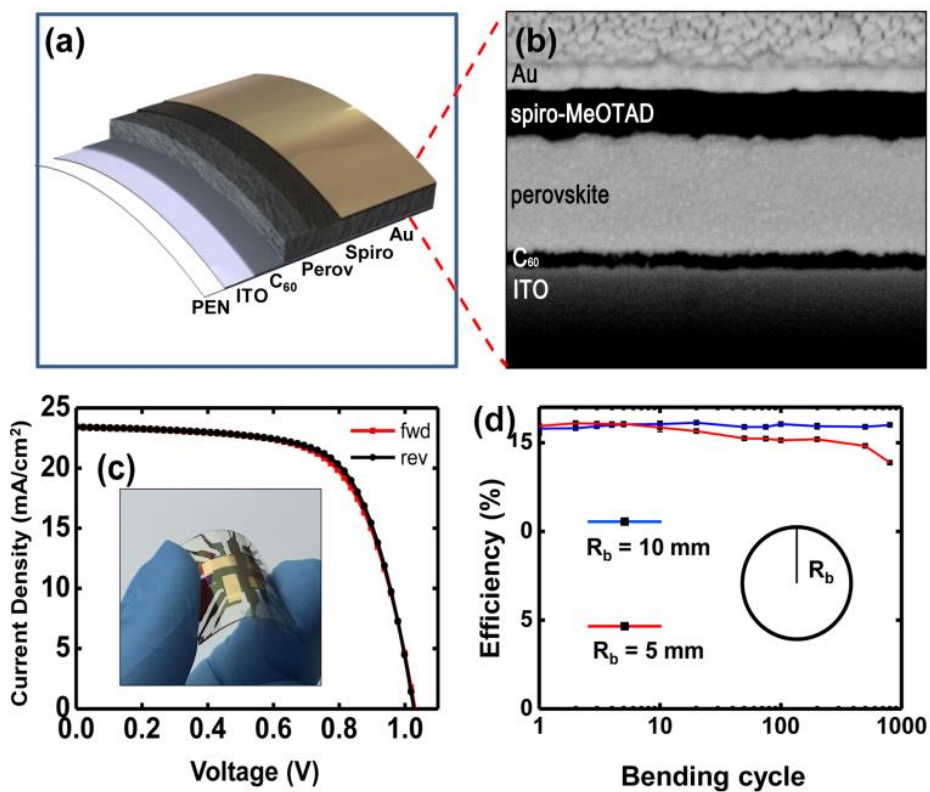


**Figure 3.9** (a) The structure of flexible MAPbI<sub>3</sub> perovskite solar cell on a PEN/ITO substrate. (b) Cross sectional FE-SEM Image of a flexible MAPbI<sub>3</sub> perovskite solar cell (c) J-V characteristics of the perovskite cell. The Inset shows a digital camera image of the fabricated MAPbI<sub>3</sub> perovskite solar cell (d) Efficiency of flexible perovskite devices as a function of bending cycles with different radii of 10 mm and 5 mm.  $R_b$  is the radius of curvature

	$V_{oc}$ (V)	$J_{sc}$ (mA/c m <sup>2</sup> )	Fill Factor (%)	PCE (%)
Flexible cell	1.01 ± 0.02	23.69 ± 0.43	64.98 ± 2.14	15.52 ± 0.43

**Table 3.2** Summary of the average performance of the CH<sub>3</sub>NH<sub>3</sub>PbI<sub>3</sub> perovskite devices incorporating C<sub>60</sub> layer on flexible substrate.

### 3.4. Conclusions

A hysteresis-free planar perovskite solar cell with the PCE of 19.1% was developed by using a room-temperature vacuum-processed C<sub>60</sub> as an ETL. With a thickness of 35 nm, the fabricated CH<sub>3</sub>NH<sub>3</sub>PbI<sub>3</sub> device shows the best PCE with the device parameters such as  $J_{sc}$  of 23.7 mA/cm<sup>2</sup>,  $V_{oc}$  of 1.1 V, and FF of 74.0%. The slight decrease in transmittance with increasing the thickness of C<sub>60</sub> layer up to 35 nm has no appreciable change in  $J_{sc}$ , while the  $V_{oc}$  and FF are increased due to the improved electron transport property and the reduced leakage loss. Also, the device with the C<sub>60</sub> layer showed better performance, due to better electron transporting rate, than the one adopting interface layers of the C<sub>60</sub>/BCP. Furthermore, a hysteresis-free flexible perovskite solar cell fabricated on a PEN substrate with the PCE of 16.0% was firstly demonstrated by using the same processes. Thus, the presented work can be regarded as an effective and promising method for realizing high performance flexible perovskite solar cells without hysteresis.

### 3.5. References

- [1] Burschka, J., Pellet, N., Moon, S.-J., Humphry-Baker, R., Gao, P., Nazeeruddin, M. K., & Grätzel, M. (2013). Sequential deposition as a route to high-performance perovskite-sensitized solar cells. *Nature*, 499(7458), 316.
- [2] Dong, Q., Fang, Y., Shao, Y., Mulligan, P., Qiu, J., Cao, L., & Huang, J. (2015). Electron-hole diffusion lengths > 175  $\mu\text{m}$  in solution-grown  $\text{CH}_3\text{NH}_3\text{PbI}_3$  single crystals. *Science*, 347(6225), 967-970.
- [3] Gong, J., Darling, S. B., & You, F. (2015). Perovskite photovoltaics: life-cycle assessment of energy and environmental impacts. *Energy & Environmental Science*, 8(7), 1953-1968.
- [4] Jung, H. S., & Park, N. G. (2015). Perovskite solar cells: from materials to devices. *small*, 11(1), 10-25.
- [5] Kim, H.-S., Lee, C.-R., Im, J.-H., Lee, K.-B., Moehl, T., Marchioro, A., . . . Moser, J. E. (2012). Lead iodide perovskite sensitized all-solid-state submicron thin film mesoscopic solar cell with efficiency exceeding 9%. *Scientific reports*, 2, 591.
- [6] Lee, M. M., Teuscher, J., Miyasaka, T., Murakami, T. N., & Snaith, H. J. (2012). Efficient hybrid solar cells based on meso-superstructured organometal halide perovskites. *Science*, 338(6107), 643-647.
- [7] Shi, D., Adinolfi, V., Comin, R., Yuan, M., Alarousu, E., Buin, A., . . . Katsiev, K. (2015). Low trap-state density and long carrier diffusion in organolead trihalide perovskite single crystals. *Science*,

- 347(6221), 519-522.
- [8] Stranks, S. D., Eperon, G. E., Grancini, G., Menelaou, C., Alcocer, M. J., Leijtens, T., . . . Snaith, H. J. (2013). Electron-hole diffusion lengths exceeding 1 micrometer in an organometal trihalide perovskite absorber. *Science*, 342(6156), 341-344.
- [9] Sung, H., Ahn, N., Jang, M. S., Lee, J. K., Yoon, H., Park, N. G., & Choi, M. (2016). Transparent Conductive Oxide-Free Graphene-Based Perovskite Solar Cells with over 17% Efficiency. *Advanced Energy Materials*, 6(3), 1501873.
- [10] Xing, G., Mathews, N., Sun, S., Lim, S. S., Lam, Y. M., Grätzel, M., . . . Sum, T. C. (2013). Long-range balanced electron-and hole-transport lengths in organic-inorganic CH<sub>3</sub>NH<sub>3</sub>PbI<sub>3</sub>. *Science*, 342(6156), 344-347.
- [11] Kojima, A., Teshima, K., Shirai, Y., & Miyasaka, T. (2009). Organometal halide perovskites as visible-light sensitizers for photovoltaic cells. *Journal of the American Chemical Society*, 131(17), 6050-6051.
- [12] [http://www.nrel.gov/ncpv/images/efficiency\\_chart.jpg](http://www.nrel.gov/ncpv/images/efficiency_chart.jpg)
- [13] Ball, J. M., Lee, M. M., Hey, A., & Snaith, H. J. (2013). Low-temperature processed meso-superstructured to thin-film perovskite solar cells. *Energy & Environmental Science*, 6(6), 1739-1743.
- [14] Heo, J. H., Im, S. H., Noh, J. H., Mandal, T. N., Lim, C. S., Chang, J. A., ... & Grätzel, M. (2013). Efficient inorganic–organic hybrid heterojunction solar cells containing perovskite compound and polymeric hole conductors. *Nature photonics*, 7(6), 486.

- [15] Eperon, G. E., Burlakov, V. M., Docampo, P., Goriely, A., & Snaith, H. J. (2014). Morphological control for high performance, solution-processed planar heterojunction perovskite solar cells. *Advanced Functional Materials*, 24(1), 151-157.
- [16] Park, N. G. (2013). Organometal perovskite light absorbers toward a 20% efficiency low-cost solid-state mesoscopic solar cell. *The Journal of Physical Chemistry Letters*, 4(15), 2423-2429.
- [17] Zhou, H., Chen, Q., Li, G., Luo, S., Song, T. B., Duan, H. S., ... & Yang, Y. (2014). Interface engineering of highly efficient perovskite solar cells. *Science*, 345(6196), 542-546.
- [18] Tao, C., Neutzner, S., Colella, L., Marras, S., Kandada, A. R. S., Gandini, M., ... & Bertarelli, C. (2015). 17.6% stabilized efficiency in low-temperature processed planar perovskite solar cells. *Energy & Environmental Science*, 8(8), 2365-2370.
- [19] Snaith, H. J., Abate, A., Ball, J. M., Eperon, G. E., Leijtens, T., Noel, N. K., ... & Zhang, W. (2014). Anomalous hysteresis in perovskite solar cells. *J. Phys. Chem. Lett*, 5(9), 1511-1515.
- [20] Unger, E. L., Hoke, E. T., Bailie, C. D., Nguyen, W. H., Bowring, A. R., Heumüller, T., ... & McGehee, M. D. (2014). Hysteresis and transient behavior in current–voltage measurements of hybrid-perovskite absorber solar cells. *Energy & Environmental Science*, 7(11), 3690-3698.
- [21] Li, Y., Zhao, Y., Chen, Q., Yang, Y., Liu, Y., Hong, Z., ... & Yang, Y. (2015). Multifunctional fullerene derivative for interface engineering in perovskite solar cells. *Journal of the American Chemical Society*, 137(49), 15540-15547.

- [22] Docampo, P., Ball, J. M., Darwich, M., Eperon, G. E., & Snaith, H. J. (2013). Efficient organometal trihalide perovskite planar-heterojunction solar cells on flexible polymer substrates. *Nature communications*, 4, 2761.
- [23] Seo, J., Park, S., Kim, Y. C., Jeon, N. J., Noh, J. H., Yoon, S. C., & Seok, S. I. (2014). Benefits of very thin PCBM and LiF layers for solution-processed p-i-n perovskite solar cells. *Energy & Environmental Science*, 7(8), 2642-2646.
- [24] You, J., Hong, Z., Yang, Y., Chen, Q., Cai, M., Song, T. B., ... & Yang, Y. (2014). Low-temperature solution-processed perovskite solar cells with high efficiency and flexibility. *ACS nano*, 8(2), 1674-1680.
- [25] Heo, J. H., Han, H. J., Kim, D., Ahn, T. K., & Im, S. H. (2015). Hysteresis-less inverted CH<sub>3</sub>NH<sub>3</sub>PbI<sub>3</sub> planar perovskite hybrid solar cells with 18.1% power conversion efficiency. *Energy & Environmental Science*, 8(5), 1602-1608.
- [26] Liu, Y., Bag, M., Renna, L. A., Page, Z. A., Kim, P., Emrick, T., ... & Russell, T. P. (2016). Understanding interface engineering for high-performance fullerene/perovskite planar heterojunction solar cells. *Advanced Energy Materials*, 6(2), 1501606.
- [27] Shao, Y., Xiao, Z., Bi, C., Yuan, Y., & Huang, J. (2014). Origin and elimination of photocurrent hysteresis by fullerene passivation in CH<sub>3</sub>NH<sub>3</sub>PbI<sub>3</sub> planar heterojunction solar cells. *Nature communications*, 5, 5784.
- [28] Abrusci, A., Stranks, S. D., Docampo, P., Yip, H. L., Jen, A. K. Y., & Snaith, H. J. (2013). High-performance perovskite-polymer

- hybrid solar cells via electronic coupling with fullerene monolayers. *Nano letters*, 13(7), 3124-3128.
- [29] Liang, P. W., Chueh, C. C., Williams, S. T., & Jen, A. K. Y. (2015). Roles of fullerene-based interlayers in enhancing the performance of organometal perovskite thin-film solar cells. *Advanced Energy Materials*, 5(10), 1402321.
- [30] Bi, C., Yuan, Y., Fang, Y., & Huang, J. (2015). Low-Temperature Fabrication of Efficient Wide-Bandgap Organolead Trihalide Perovskite Solar Cells. *Advanced Energy Materials*, 5(6), 1401616.
- [31] Li, Y., Ye, S., Sun, W., Yan, W., Li, Y., Bian, Z., ... & Huang, C. (2015). Hole-conductor-free planar perovskite solar cells with 16.0% efficiency. *Journal of Materials Chemistry A*, 3(36), 18389-18394.
- [32] Wojciechowski, K., Leijtens, T., Siprova, S., Schlueter, C., Hörantner, M. T., Wang, J. T. W., ... & Snaith, H. J. (2015). C60 as an efficient n-type compact layer in perovskite solar cells. *The journal of physical chemistry letters*, 6(12), 2399-2405.
- [33] Ke, W., Zhao, D., Grice, C. R., Cimaroli, A. J., Ge, J., Tao, H., ... & Yan, Y. (2015). Efficient planar perovskite solar cells using room-temperature vacuum-processed C 60 electron selective layers. *Journal of Materials Chemistry A*, 3(35), 17971-17976.
- [34] Cao, W., & Xue, J. (2014). Recent progress in organic photovoltaics: device architecture and optical design. *Energy & Environmental Science*, 7(7), 2123-2144.
- [35] Xue, J., Uchida, S., Rand, B. P., & Forrest, S. R. (2004). Asymmetric tandem organic photovoltaic cells with hybrid planar-

- mixed molecular heterojunctions. *Applied Physics Letters*, 85(23), 5757-5759.
- [36] Pfuetzner, S., Meiss, J., Petrich, A., Riede, M., & Leo, K. (2009). Improved bulk heterojunction organic solar cells employing C 70 fullerenes. *Applied Physics Letters*, 94(22), 145.
- [37] Peumans, P., Bulović, V., & Forrest, S. R. (2000). Efficient photon harvesting at high optical intensities in ultrathin organic double-heterostructure photovoltaic diodes. *Applied Physics Letters*, 76(19), 2650-2652.
- [38] Park, I. J., Park, M. A., Kim, D. H., Park, G. D., Kim, B. J., Son, H. J., ... & Park, N. G. (2015). New hybrid hole extraction layer of perovskite solar cells with a planar p-i-n Geometry. *The Journal of Physical Chemistry C*, 119(49), 27285-27290.
- [39] Kim, B. J., Kim, D. H., Lee, Y. Y., Shin, H. W., Han, G. S., Hong, J. S., ... & Park, N. G. (2015). Highly efficient and bending durable perovskite solar cells: toward a wearable power source. *Energy & Environmental Science*, 8(3), 916-921.

## **Chapter 4.**

# **Graphene-based Hybrid Electrode for Flexible Electronics**

---

### **4.1. Introduction**

Emergence of methyl ammonium lead trihalide ( $\text{CH}_3\text{NH}_3\text{PbI}_3 = \text{MAPbI}_3$ ) perovskite has provoked a lucrative research area of photovoltaic market due to its low materials cost, easy solution processability and scalability while exhibiting tremendous improvement in its power conversion efficiency [1,2]. This typical light absorber with superior photo-physical properties, such as efficient light absorption, extremely long ambipolar carrier diffusion lengths, allows to enormously increase in its power conversion efficiency (PCE) over 20% [3,4]. Although a crucial potential of perovskite solar cells over silicon photovoltaics is the capability of scalable fabrication of active materials that can be deposited on diverse flexible substrates by utilizing large-area coating techniques such as slot-die, inkjet, spray,

spin-coating etc. [1,3-8], however, indium tin oxide (ITO) or fluorine doped tin oxide (FTO), most commonly used conductive oxide transparent electrodes in optoelectronics, hinder the process due to their brittle nature of ceramic making it incompatible. To overcome intrinsic limitation of conducting oxides for integration of scalable fabrication techniques, many alternative flexible transparent conducting materials have been explored including thin film metal grid, conducting polymer, carbon nanotubes, metal nanowires percolation network, electro-spun metal fibers and graphene as transparent electrodes for optoelectronic applications [9-18].

Furthermore, hybrid electrodes with a combination of proposed alternatives and existing conductive oxides also have been extensively researched for perovskite solar cells [11,13,19]. Since each materials experience own limitations as a flexible transparent electrode, hybrid structures suggest solutions by drawing advantages of each materials and embracing their characteristics properly. In many choices, monolithically grown single crystal graphene is one of attractive material due to its chemical stability as a carbon material, mechanical super-flexibility of monolithic structure and high optical transparency (<97%) [20]. However, since its electrical property is critically

dependent on its grain-size grown by precisely controlled chemical vapor deposition process, when it comes to fabricate the electrode in a large area, the electrical performance of graphene as an electrode becomes inadequate to apply for large-area photovoltaic [18]. On the other hand, silver nanowires (Ag NW) based transparent electrode shows the remarkable electrical and optical properties and easy solution-processability over a large area among any other candidates [20]. Nevertheless, because of common oxidation problem of metals and corrosion problem caused by chemical volatility of silver to iodine ions from perovskite layer, the protection of Ag NW electrode film must be inevitably achieved [20-22].

Therefore, here, we propose a method to fabricate a large area hybrid transparent electrode by incorporating advantages of monolithic graphene layer and silver nanowires (Ag NW) percolation network. Monolithic graphene layer protects Ag NW percolation network from oxidative and chemically volatile environment at the top of the electrode and gives electrical pathways in lateral directions covering voids that Ag NW percolation network unavoidably possesses for effective extraction of excitons [23]. At the same time, Ag NW percolation network positioned under the graphene layer provides

electrical highways that pass most of grain boundaries of monolithic graphene layer over a large area to carry out fast charge collection [20,24]. In addition, the embedment of hybrid electrode in spin-coated ultra-thin Teflon, or polytetrafluoroethylene (PTFE) polymer matrix, offers compact binding of heterogeneous conductive materials as well as smooth surface while chemically immiscible to high polarity solvents when the electrode is exposed. Lastly, adoption of megasonic spraying system to the hybrid electrode enables the demonstration of a large area p-i-n structured perovskite solar cell [25]. The roughness rms of less than 5 nm uniformly stacks each layer of perovskite solar cell despite which method is used. The specifics of the hybrid electrode are very similar with that of ITO. The sheet resistance of the hybrid electrode is 10.7 ohm/sq while that of ITO is 10.12 ohm/sq. The average transmittance between 350 nm ~ 800 nm range of spectrum is 87.1% while that of ITO is 91.18%. Thus, the development of the hybrid graphene/Ag NW electrode in a large area will give an opportunity to take a closer step to realize commercialization of perovskite solar cells, to replace high performance silicon based solar cells at a low cost and high performance with scalable fabrication process.

## 4.2. Experimental Methods

### 4.2.1. Synthesis of Ag NW

In this typical synthesis of Ag NW, the amounts of all reagent chemicals were precisely controlled by previously introduced polyol methods [23]. In ethylene glycol, polyvinylpyrrolidone (Molecular weight ~360,000) and silver nitrate ( $\text{AgNO}_3$ ) were sequentially dissolved in a triangular flask using a magnetic stirrer. Once thorough dissolution of all solutes was achieved, the stirrer was carefully removed from the mixture solution. Then,  $\text{CuCl}_2 \cdot 2\text{H}_2\text{O}$  (3.3 mM) was rapidly injected into the mixture and stirred gently for 1 min. Finally, the mixture solution was suspended in a preheated silicone oil bath at  $130^\circ\text{C}$  for the growth of Ag NW and maintained at the elevated temperature for 3 h. The synthesized Ag NW in the resultant solution were first agglomerated using acetone, and then re-dispersed in ethanol to remove organic chemical residues on the NW surface with centrifugation at 3000 rpm for 10 min. This process was repeated three to four times to obtain a very long Ag NW percolation network with

high-quality. The materials used for Ag NW synthesis were purchased from Sigma-Aldrich.

#### 4.2.2. Synthesis of 2L Graphene/copper film

2L Graphene on copper foil (graphene Square Inc.) is obtained by stacking a monolayer graphene on top of synthesized graphene on copper foil. Monolayer graphene synthesis was synthesized on a Cu catalyst by CVD. The 25  $\mu\text{m}$  thick Cu foil was inserted into a quartz tube and then heated up to 1000°C at the ambient pressure with a flow  $\text{H}_2$  and Ar. After flowing reaction gas mixtures ( $\text{CH}_4:\text{H}_2:\text{Ar} = 50:15:1000$  sccm) for about f min, the sample was rapidly cooled down to room temperature. After the first monolayer graphene synthesis, the supporting polymer layer of poly(methyl methacrylate) (PMMA) was spin coated on the graphene surface to protect it during the wet chemical etching process. The Cu foil was then etched by ammonium persulphate ( $(\text{NH}_4)_2\text{S}_2\text{O}_8$ ) solution, followed by rinsing with deionized water. PMMA-supported graphene is transferred onto the second synthesized monolayer graphene on copper film through wet transfer. The PMMA layer was not removed for protection reasons.

### 4.2.3. Fabrication of Hybrid Electrode

The hybrid electrode was fabricated through multiple depositions and transfers. To support the copper foil with rigid substrate, glass (AMG, 50 x 50 mm<sup>2</sup>) / Polydimethylsiloxane (PDMS) (Down Corning Sylgard 184) was employed. PDMS was spin-coated at 3000 rpm for 30 s and cured at 70°C for 1 h. 2L graphene on copper foil was carefully transferred on glass / PDMS substrate. Then, the PMMA support layer on graphene was removed by acetone. To enhance the surface properties of graphene surface, a 2 nm-thick MoO<sub>3</sub> layer was deposited at rate of 0.1 Å/s. The deposition rate and the thickness were monitored by a quartz crystal sensor during the deposition. Ag NW dispersed in deionized water solution were dripped while the substrate was spinning at 500 rpm for 10 s followed by incremented rpm of 3000 rpm for 30 s. The substrate is, then, annealed at 180°C for 30 min to enhance the conductivity of Ag NW. Amorphous Fluoroplastic Resin (DuPont) solution was spin-coated at 500 rpm for 15 s and 1000 rpm for 30 s and dried at 70°C for 2 h.

After finishing preparation of Teflon covered sample, additional set of glass (AMG, 25 x 25 mm<sup>2</sup>) / PDMS or glass / PDMS / PET was

prepared before final transfer process. The PDMS is spin-coated with same conditions, 3000 rpm for 30 s. This substrate will be the supporting rigid substance for the whole cell.

Final sets of supporting substrates and prepared Teflon covered sample are treated with O<sub>2</sub> plasma at 100W for 2 min. Then glass primer was applied on the surface of both sets prior to spin-coating process of 3000 rpm for 1 min. the samples are annealed at 90°C for 2 min. Completed samples are manually clipped from original substrate and dry transferred to final supporting substrate facing Teflon first to the surface of the supporting substrate. Then the Cu foil was then etched by ammonium persulphate ((NH<sub>4</sub>)<sub>2</sub>S<sub>2</sub>O<sub>8</sub>) solution, followed by rinsing with deionized water. The hybrid electrode samples are dried at 100°C for 20 min. in ambient air.

#### 4.2.4. Fabrication of Perovskite Solar Cell

Fabrication of Megasonic Spray-Coated Perovskite Solar Cells: The poly(triarylamine) (PTAA, Sigma Aldrich) solution was spin-coated on the graphene & Ag NW substrates at 6000 rpm for 30 s and dried at 100 °C for 30 min. The poly[(9,9-bis(3'-(N,N-dimethylamino)propyl)-2,7-fluorene)-alt-2,7-(9,9-dioctylfluorene)] (PFN, 1-Material) solution was spin-coated on the substrates at 6000 rpm for 30s before and after the PTAA coating. The FA<sub>0.8</sub>MA<sub>0.2</sub>Pb(I<sub>2.8</sub>Br<sub>0.2</sub>) perovskite precursor solution was then deposited on the substrates using the megasonic spray system. The perovskite solution was prepared by dissolving PbI<sub>2</sub> (Alfa Aesar)/FAI (GreatCell Solar)/MABr (GreatCell Solar) (1:0.8:0.2 molar ratio) into  $\gamma$ -Butyrolactone (GBL, Junsei) at 30 wt%. The substrates were deposited on a hot-plate, situated 1 mm under the nozzle. The temperature of the substrate was 60 °C during the spraying and the flow rate of the solution was set to 15 L/min with 50 mm<sup>2</sup> of nozzle size. The deposited substrates were post-annealed at 115 °C for 1 min with DMSO vapor and 30 min in air. All megasonic spray-coating and annealing processes were carried out in a closed chemical hood under ambient conditions. For scaling up this process, a careful

control of exhaust gas flows should be needed. C<sub>60</sub> (20 nm), bathocuproine (BCP, 10 nm), and Cu (50 nm) were then sequentially deposited by thermal evaporation. In the case of the large-area (10 × 10 cm<sup>2</sup>) perovskite layer coating, sixteen substrates of 2.5 × 2.5 cm<sup>2</sup> were deposited on the hotplate, which were processed with the same conditions.

#### **4.2.5. Characterization**

The surface morphologies of the hybrid electrode and the fabricated perovskite solar cells were detected by FE-SEM (AURIGA, Carl Zeiss). The cross-sectional images of the devices were examined by focused-ion-beam assisted SEM (FIB-SEM, AURIGA, Carl Zeiss). The transmittance of various transparent electrodes was investigated by UV/Vis spectrometer (Cary 5000, Agilent technologies) in the visible range from 300 to 800 nm. J-V characteristics of the fabricated perovskite solar cells were measured with a computer-controlled Keithley 2400 source meter at room temperature inside the glove box.

## **4.3. Results and Discussion**

### **4.3.1. Structure of Hybrid Electrode Based Solar Cell**

The structure of the graphene-based hybrid electrode consisting of glass or PEN/Ag NW embedded Teflon/graphene/PTAA/perovskite/fullerene/BCP/copper is schematically illustrated in figure 4.1. Between the substrate and hybrid electrode, we used Teflon layer to completely embed Ag NW and passivate with graphene layer to form a smooth surface. Amorphous Teflon was carefully chosen to give perfectly chemically stable flexible substrate that holds hybrid electrode firmly. We adopted normal and inverted perovskite solar cell structure using PTAA and C<sub>60</sub>/BCP as the hole transporting layer (HTL) and the electron transporting layer (ETL), respectively. Every step in this structure is low-temperature processable and thus suitable for flexible perovskite solar cells and was practiced to check the compatibility of hybrid electrode and conventional flexible perovskite solar cell. A hybrid electrode composed of graphene and Ag NW was utilized as a transparent electrode because the combination can support the weakness of individual characteristics. The combination of graphene

and Ag NW lowered the sheet resistance of graphene resistance by embedding flat Ag NW layer and also guaranteed fine coverage over the vacancies of Ag NW electrode for optimum charge collection. Between the substrate and hybrid electrode, we used Teflon layer to completely embed Ag NW and passivate with graphene layer to form a smooth surface. Amorphous Teflon was carefully chosen to give perfectly chemically stable flexible substrate that holds hybrid electrode firmly.

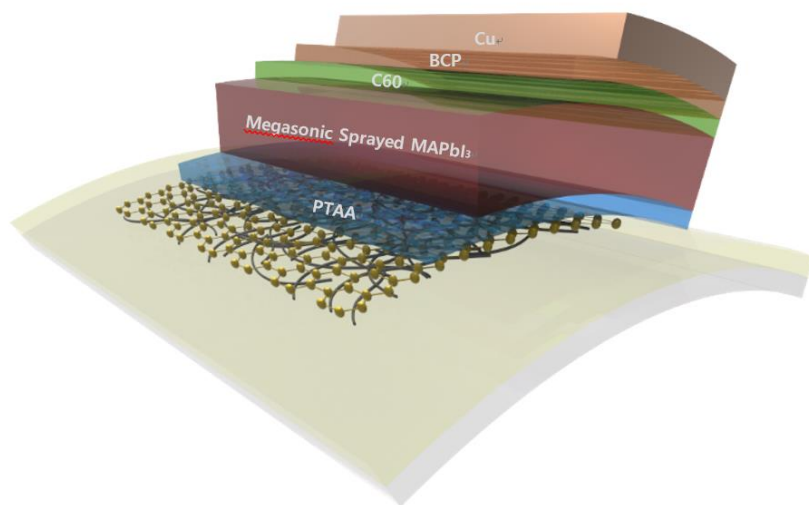


**Figure 4.1** The structure of the hybrid electrode and flexible perovskite solar cell on the hybrid electrode.

### **4.3.2. Teflon Optimization.**

Teflon is a fluorocarbon solid consisting wholly of carbon and fluorine. Teflon is hydrophobic as fluorocarbon demonstrates mitigated London dispersion forces due to the high electronegativity of fluorine. It is nonreactive due to the strength of carbon-fluorine bonds (figure 4.2). Also, Teflon is the only transparent substrate that can be utilized through spin-coating and withhold any perovskite organic solvents, which is a strong reason why it is a strong candidate for hybrid electrode despite its low surface energy. Despite its excellent experimental results as supporting transparent polymer, Teflon was still far from optimal integration with graphene and perovskite layer. First, AF Teflon is not easy to detach from glass substrate after curing process. To perfectly embed Ag NW inside Teflon polymer, Ag NW has to be aligned on a flat glass substrate followed by solution dripping of liquid amorphous Teflon. The cured Ag NW Teflon composite, then, has to be transferred and flip sides to use the flat surface that exposes Ag NW. Despite its hydrophobicity and low friction coefficient, Teflon is very well bonded to the glass substrate and is very uneasy to detach the composite layer from the substrate; Teflon needed a sacrificial layer

such as PMMA as shown in figure 4.3. Also the Teflon layer creates a unique bubbly pattern on the top surface as it goes through curing process. This pattern is permanent and leaves its mark after the transferring process.

As a result, the transferred layer has a wavy surface that affects other thermal evaporated layer and spin-coated layer resulting device failure. Figure 4.4 shows graphical process of how cell is fabricated on bubbly surfaced Teflon and the result visual data. To reduce the altitude difference caused during Teflon curing, the sample was placed under high pressure with high heat. The adhesion between Teflon layer and the substrate increased, but the bumpy is surface stayed unchanged, causing wavy surface as shown in photograph in figure 4.5. Addition to this, Teflon is a hydrophobic material that interferes wet and dry transfer process of the graphene. Wet transfer requires hydrophilic characteristics since the transfer takes place within deionized water. Hydrophobic surface causes wrinkles due to unwanted transfer in water. Low friction coefficient also causes unwanted slips during both wet and dry transfer, resulting total failure. As a result, the characteristics of Teflon required a new fabrication method to bond graphene on Teflon layer for this unique hybrid electrode.

The renovation of fabrication insured perfect bonding between two hydrophobic materials and flat surface with no problem of handling or transferring the hybrid electrode. This unique structure was done using multiple room-temperature process to overcome the limitations of bonding strength between each layer. Conventionally, Graphene layer is transferred either by wet transfer or dry transfer. Both transferring methods use surface energy difference between two substrates, normally from low surface energy substrate to high surface energy substrate, to easily move Graphene from one to another. In this study, neither method can be utilized due to low surface energy of Teflon.

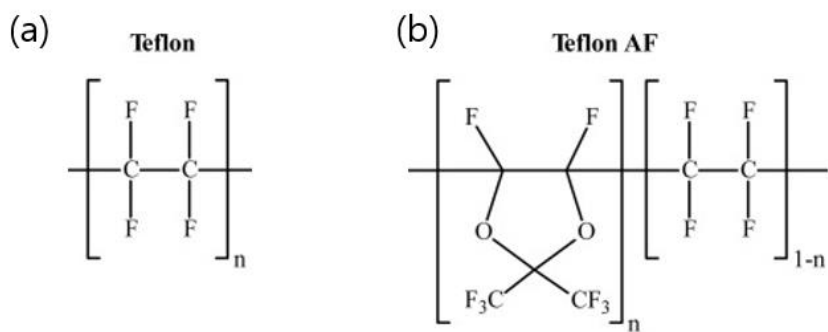


**Figure 4.2** Chemical equation comparison for amorphous Teflon and normal Teflon.

(a) Ambient condition  
24H



Bubbly surface & hard to detach from glass



(b) Easier detachment  
with sacrificial layer



**Figure 4.3** Schematic image of bubbly cured Teflon surface and its alternative process to easily detach Teflon layer by applying PMMA sacrificial layer.

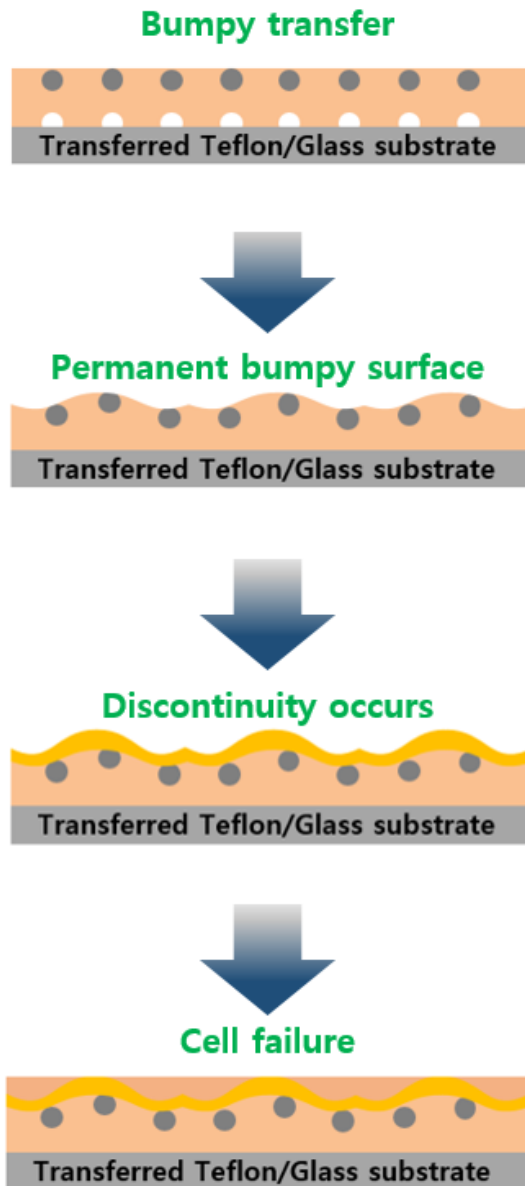


**Figure 4.4** Schematic image of transferred Teflon layer with bubbly surface and its following fabrication process effects due to its bubbly surface.

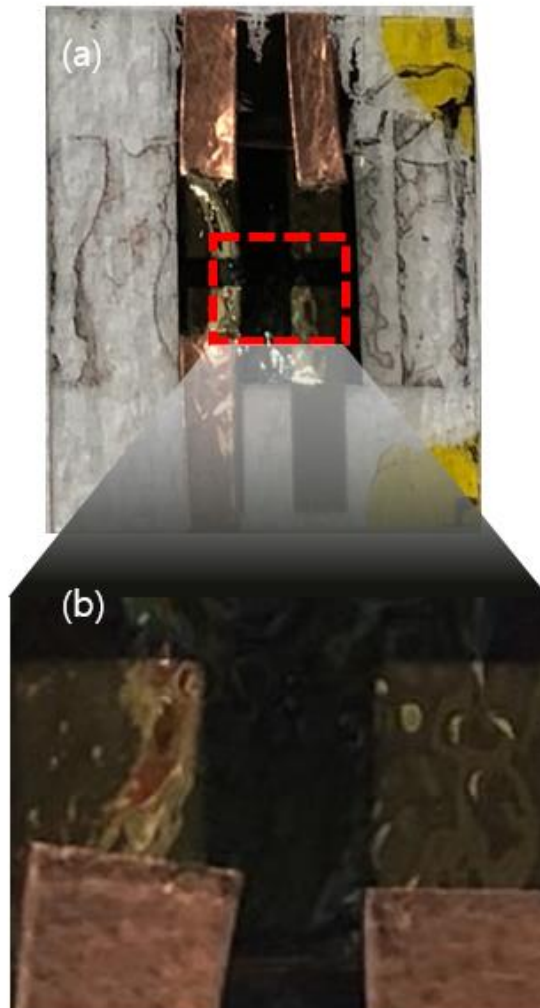


**Figure 4.5** Photographic image of the top surface of fabricated solar cell on bumpy Teflon layer. The surface morphology shows wavy top layer that is caused by the bumpy surface occurred during Teflon curing.

To successfully integrate Teflon as backbone substrate of hybrid electrode, Ag NW is directly spin-coated on graphene/copper substrate after CVD process. After strengthening the junctions of Ag NW by annealing, amorphous Teflon solution is carefully coated on Ag NW/graphene/Cu. The thickness of Teflon is a key factor in fabricating a flat electrode. Thin layer of Teflon cannot fully cover Ag nanowires and result rough surface. Thick layer of Teflon can also result rough surface since Teflon has its natural characteristic to form bumpy surface as the phase changes from liquid to solid. Due to low coefficients of friction, the liquid phase of Teflon is easily detached from the substrate during normal spin-coating. As shown in figure 4.6, various methods from simply dripping, to spin-coating were compared to select a right method when coating Teflon layer. To form a fully covered substrate, an excess amount of liquid Teflon is applied while spinning the substrate at a low speed of 500 rpm. The optimized spin-coating process fully covers nanowires with enough liquid Teflon, resulting flat nanowire-embedded surface.

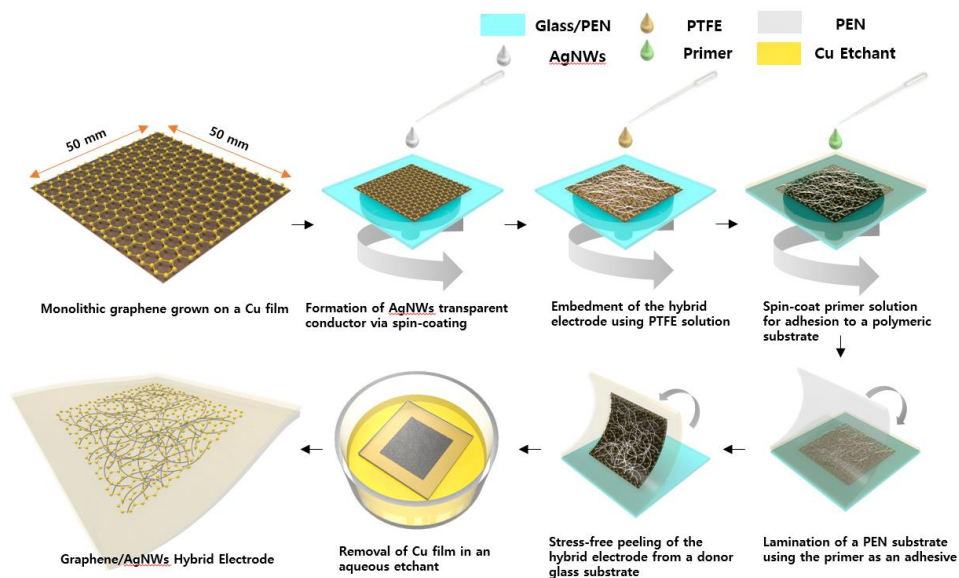


**Figure 4.6** Schematic process of fabrication of the hybrid electrode. CVD processed graphene on copper foil was attached on rigid glass followed by Ag NW and AF Teflon deposition through spin-coating method. Then, primer is coated on the surface of Teflon layer to attach final substrate, PEN or glass. The hybrid electrode is detached from initial glass substrate. Copper foil is removed in metal etchant bath.

Cured substrate is then attached to clear glass/PEN substrate by applying glass primer on both glass/PEN and Teflon surface. Finalized substrate is dipped in metal etching agent to eliminate copper top layer. The copper layer protects Graphene from external factors until the final process of fabrication. The graphene layer safely protects Ag NW from metal etchant, allowing only copper layer to be removed during etching process. As a result, we were able to fabricate a large area flat-surfaced Graphene-Ag NW hybrid transparent electrode as shown in figure 4.7. The transparency and sheet resistance of the electrode was controlled by the concentration of Ag NW.

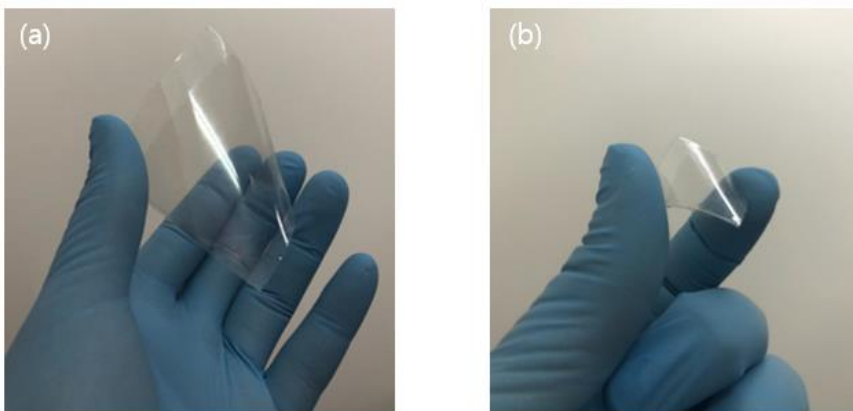


**Figure 4.7** Photographic image of the hybrid electrode on (a) 40 mm X 40 mm flexible substrate and (b) 25 mm X 25 mm flexible substrate.

### 4.3.3. Conductivity and Transparency Optimization

Figure 4.8(a) and (b) show the transmittance and sheet resistance of Ag NW due to various concentrations. Our goal for this study is to utilize Ag NW and fabricate a hybrid electrode that performs like ITO. Therefore, we diluted the concentration to match the sheet resistance of Ag NW to that of ITO, which is around 10 ohm/sq with concentration of 0.1 wt%. Figure 4.9 shows the transmittance comparison of ITO, Ag NW, and hybrid electrode. For both Ag NW and hybrid electrode, the concentration of Ag NW was 0.1 wt%. The Ag NW shows average transmittance of 90.97% between 350 nm~800 nm spectrum while ITO showed very similar 91.18%. The hybrid electrode showed 87.17% with same visual condition. Considering how hybrid electrode has graphene with multi-stacked transparent polymer layers, the hybrid electrode has shown superb performance. As stated on the objectives, the sheet resistance of the hybrid electrode matched that of the ITO electrode. The sheet resistance measurements are listed on table 4.1.

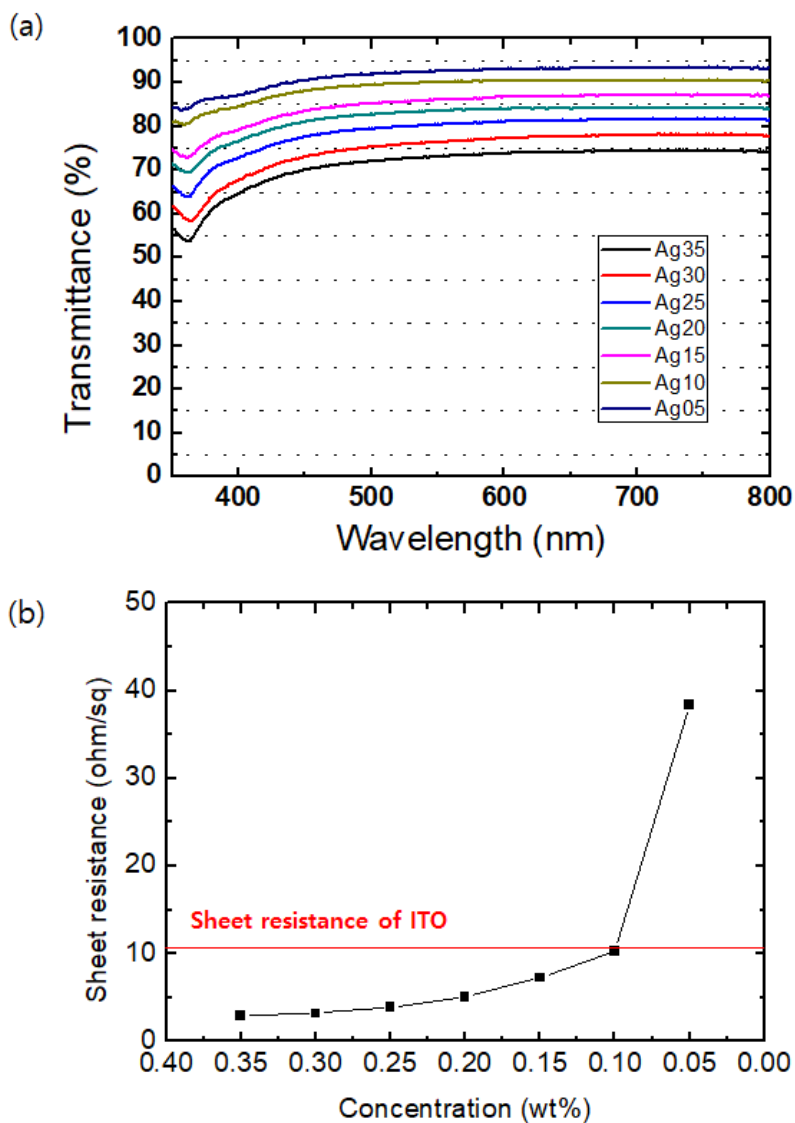


**Figure 4.8** (a) Transmittance and sheet resistance comparison for different concentration of Ag NW. The transmittance and sheet resistance are inversely proportional to each other. Ag NW of 0.1 wt% is used since the sheet resistance of 0.1 wt% is the closest to that of ITO.

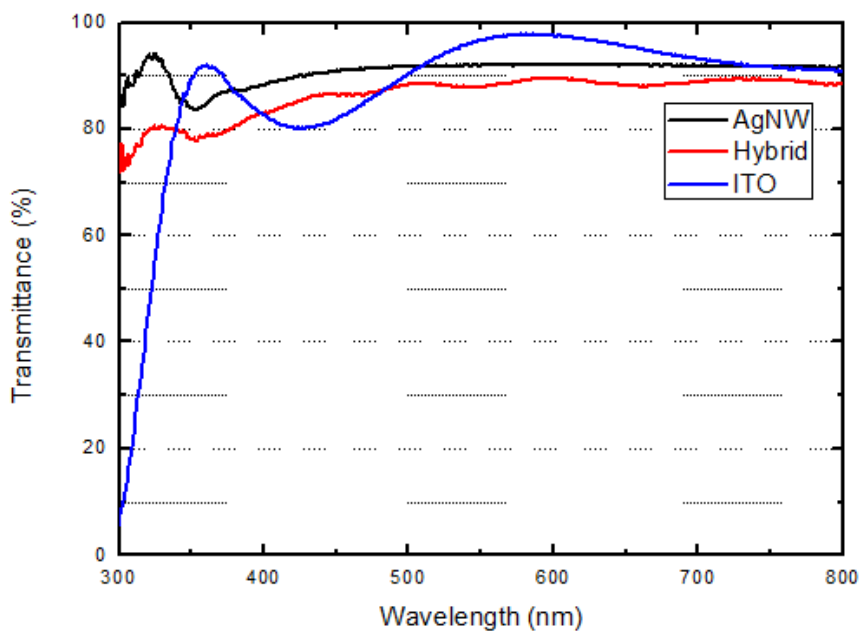


**Figure 4.9** Transmittance comparison for different electrode materials. For Ag NW and hybrid electrode, 0.1 wt% of Ag NW was used. The average transmittance results between 350 nm ~ 800 nm for ITO, Ag NW, and hybrid electrode are 91.18%, 90.97%, and 87.1% respectively.

Material	Sheet resistance (ohm/sq)
Ag NW	10.23 ohm/sq
Hybrid	10.7 ohm/sq
ITO	10.12 ohm/sq

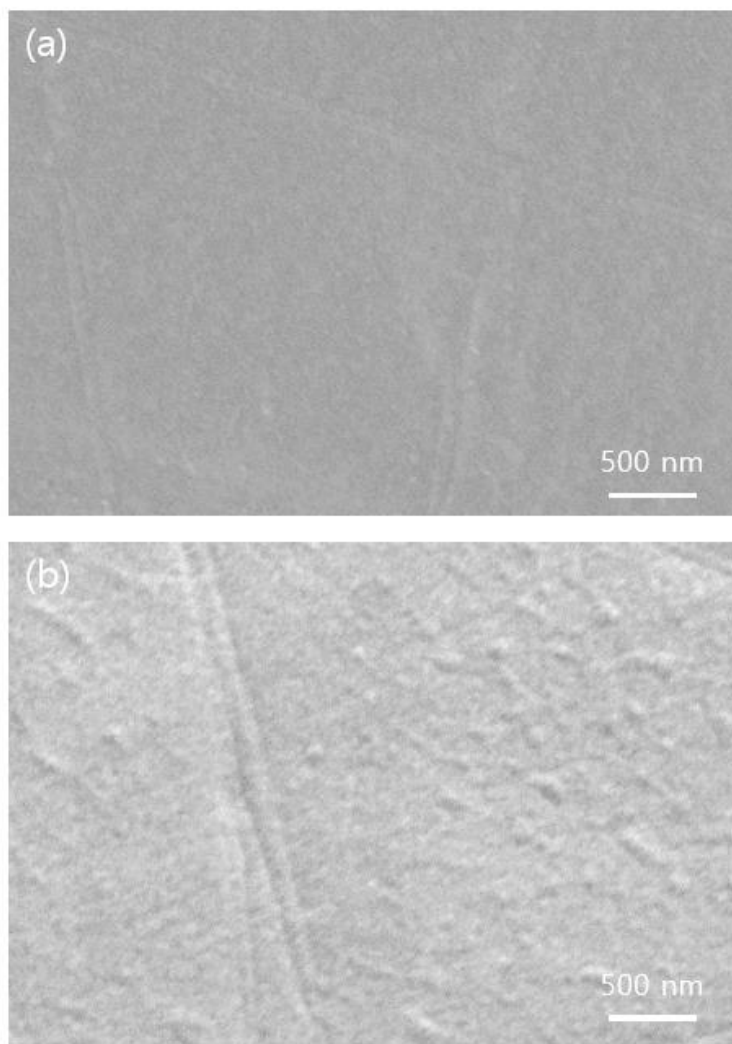
**Table 4.1** Sheet resistance for each type of electrodes.

#### 4.3.4. Characterization of Hybrid Electrode

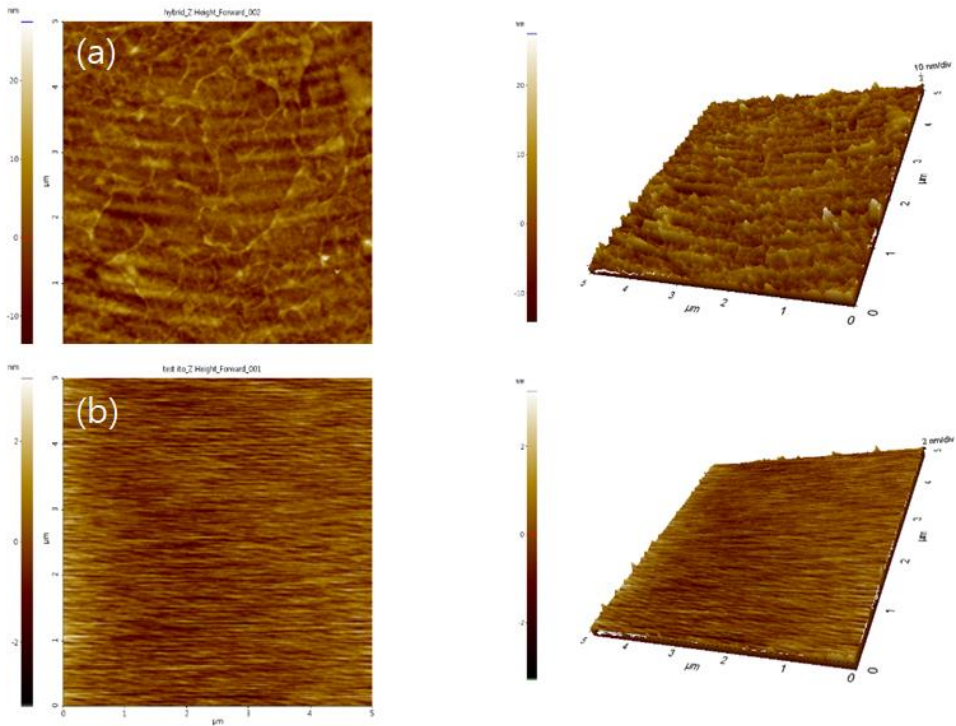
Figure 4.10(a) and (b) shows the SEM image of the hybrid electrode. Both flat and tilted image was taken to compare the visual roughness of the surface through SEM. The graphical contrast of the image on both images implies the hybrid electrode has flat surface. Additionally figure 4.11 and table 4.2 insure the flatness of the hybrid electrode by showing the AFM image of the hybrid electrode with comparative reference sample, ITO. The electrode no longer suffers from rough altitude due to Ag NW as seen in earlier models. The wavy wrinkles may occur from multiple transfers, but the overall roughness is very flat. The root mean square of hybrid electrode is 4.1 nm. Compare to bumpy roughness of few hundred nanometers seen in earlier model, the hybrid electrode can now be considered flat and cause no troubles regarding surface roughness.

Figure 4.12 compares the resistance change of hybrid electrode and ITO on PEN substrate. The hybrid electrode was bent to a radius of 5 mm with no corresponding increase in resistance, whereas the resistance of the ITO electrode increased by three orders of magnitude under the same bending radius. The results confirmed that the hybrid

electrode is extremely flexible due to the use of Graphene and silver nanowire along with flexible supporting polymer.



**Figure 4.10** Surface SEM image of the hybrid electrode on flat and 30° tilted angle. The contrast between two images and the contrast within the same image is very minimal and implies Ag NW is perfectly embedded inside the polymer.



**Figure 4.11** AFM images of both (a) hybrid electrode and (b) ITO. The hybrid electrode do show wrinkles on the surface, but overall the flatness is confirmed and Ag NW is untraceable.

	Middle (nm)	Mean (nm)	Rms (nm)
Hybrid	6.63	0	4.099
ITO	-0.014	-0.004	0.658

**Table 4.2** Statistical data from AFM measurement for hybrid electrode and ITO. Unlike ITO, the hybrid electrode do show difference between mid and mean value, but the values are still under 10 nm, confirming its flatness.

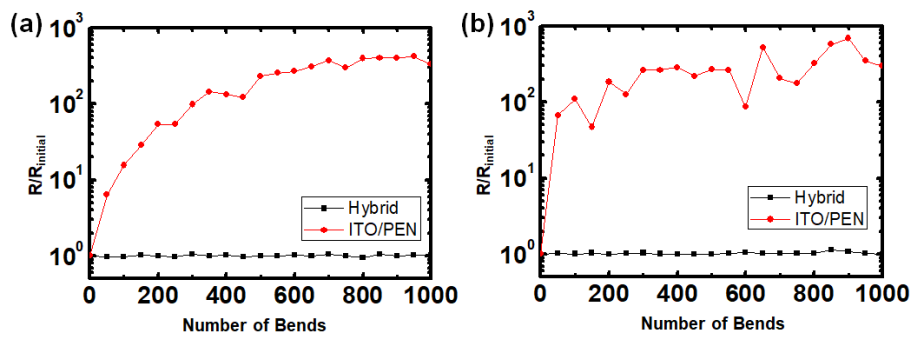


**Figure 4.12** Increase in resistance versus number of bends for the hybrid electrode and ITO on PEN substrate due to (a) 10 mm and (b) 5 mm bending radius.

#### 4.3.5. Surface Compatibility Enhancement and its Applications

The hybrid electrode has proven its excellence in physical and electrical aspect compare to that of ITO. Recalling the properties of graphene and Teflon, the hybrid electrode has hydrophobic surface that could prevent its application compatibility with other layers such as perovskite. Hydrophobic surface will reflect any solution processed materials despite what method is used. polyelectrolyte, (9,9-bis(3-(N,N-dimethylamino)propyl)-2,7-fluorene)-alt-2,7-(9,9-dioctylfluorene) (PFN), is a surface treatment material known to help increase the compatibility of the surface with any adjacent layer [27]. It can be applied on both ETL and HTL of perovskite solar cell and have no distinct difference in performance. The hybrid electrode is treated with PFN to increase its compatibility with other transporting layers and perovskite layers. Figure 4.13 shows the contact angle comparison of the hybrid electrode before and after PFN treatment. The average contact angle dropped from 110° to 93°. Although 93° still seems high, the hybrid electrode was able to bond firmly with perovskite layer. Figure 4.14 shows the cross-section SEM image of perovskite solar cell fabricated with both spin-coating method and megasonic spray method.

The electrode maintained its flat surface. Each layer is sequentially stacked on top of each layer.

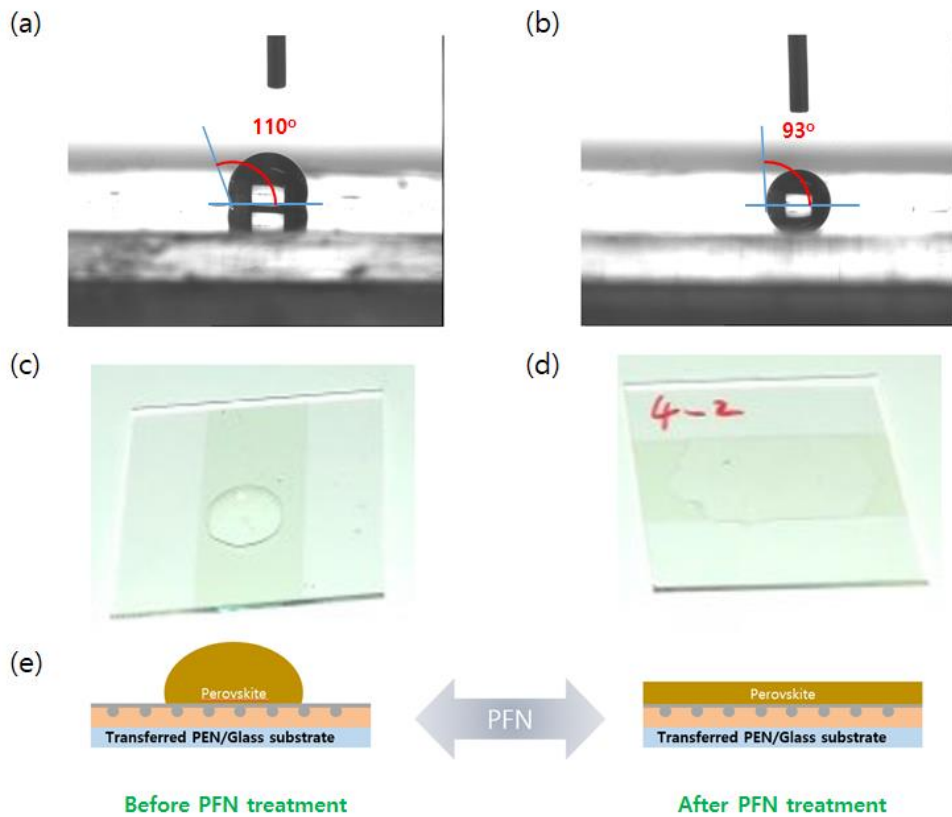
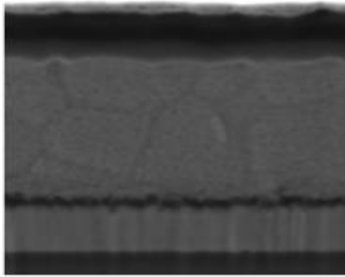
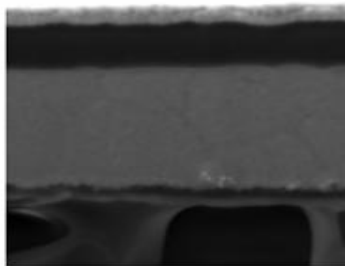


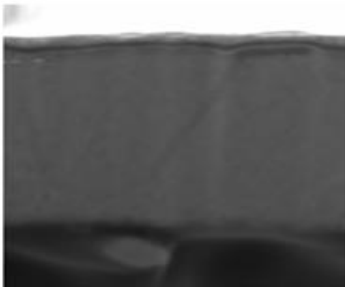
**Figure 4.13** Visual data of surface treatment with PFN on the hybrid electrode. The contact angle of the hybrid electrode decreased from (a) 110° to (b) 93°. (c) and (d) compares the visual after dripping organic solvent on the hybrid electrode. The surface treatment enabled further perovskite fabrication on the hybrid electrode.



ITO substrate  
spin-coating processed



Hybrid electrode  
spin-coating processed



Hybrid electrode  
spray-coating processed

**Figure 4.14** Cross-sectional SEM image for ITO and hybrid electrodes after full perovskite cell fabrication. PFN treatment successfully enabled perovskite layer fabrication through both spin-coating and spray methods.

## **4.4. Conclusion**

We have fabricated a hybrid electrode consisting of graphene and Ag NW. New fabricating method enabled a bond between two hydrophobic layers while ensuring perfectly flat surface. This electrode not only performs similar to that of ITO, but also overcame the limitation of conventional graphene electrode and Ag NW electrode. The graphene hybrid electrode can now cover large area with no performance loss and ensure its conductivity by embedded Ag NW under graphene passivation.

This hybrid electrode has not only shown its excellence in performance within perovskite solar cell, but also shown its potential to be integrated in various optical research/industrial areas.

## 4.5. References

- [1] You, J., Meng, L., Song, T. B., Guo, T. F., Yang, Y. M., Chang, W. H., ... & Liu, Y. (2016). Improved air stability of perovskite solar cells via solution-processed metal oxide transport layers. *Nature nanotechnology*, 11(1), 75.
- [2] Chen, Q., Zhou, H., Hong, Z., Luo, S., Duan, H. S., Wang, H. H., ... & Yang, Y. (2013). Planar heterojunction perovskite solar cells via vapor-assisted solution process. *Journal of the American Chemical Society*, 136(2), 622-625.
- [3] Kim, H. S., Lee, C. R., Im, J. H., Lee, K. B., Moehl, T., Marchioro, A., ... & Grätzel, M. (2012). Lead iodide perovskite sensitized all-solid-state submicron thin film mesoscopic solar cell with efficiency exceeding 9%. *Scientific reports*, 2, 591.
- [4] Yang, W. S., Park, B. W., Jung, E. H., Jeon, N. J., Kim, Y. C., Lee, D. U., ... & Seok, S. I. (2017). Iodide management in formamidinium-lead-halide-based perovskite layers for efficient solar cells. *Science*, 356(6345), 1376-1379.
- [5] Gheno, A., Huang, Y., Bouclé, J., Ratier, B., Rolland, A., Even, J., & Vedraïne, S. (2018). Toward Highly Efficient Inkjet-Printed Perovskite Solar Cells Fully Processed Under Ambient Conditions and at Low Temperature. *Solar RRL*, 2(11), 1800191.
- [6] Ciro, J., Mejía-Escobar, M. A., & Jaramillo, F. (2017). Slot-die processing of flexible perovskite solar cells in ambient conditions. *Solar Energy*, 150, 570-576.
- [7] Barrows, A. T., Pearson, A. J., Kwak, C. K., Dunbar, A. D.,

- Buckley, A. R., & Lidzey, D. G. (2014). Efficient planar heterojunction mixed-halide perovskite solar cells deposited via spray-deposition. *Energy & Environmental Science*, 7(9), 2944-2950.
- [8] Das, S., Yang, B., Gu, G., Joshi, P. C., Ivanov, I. N., Rouleau, C. M., ... & Xiao, K. (2015). High-performance flexible perovskite solar cells by using a combination of ultrasonic spray-coating and low thermal budget photonic curing. *Acs Photonics*, 2(6), 680-686.
- [9] Jung, E. D., Nam, Y. S., Seo, H., Lee, B. R., Yu, J. C., Lee, S. Y., ... & Song, M. H. (2015). Highly efficient flexible optoelectronic devices using metal nanowire-conducting polymer composite transparent electrode. *Electronic Materials Letters*, 11(5), 906-914.
- [10] Sung, H., Ahn, N., Jang, M. S., Lee, J. K., Yoon, H., Park, N. G., & Choi, M. (2016). Transparent Conductive Oxide-Free Graphene-Based Perovskite Solar Cells with over 17% Efficiency. *Advanced Energy Materials*, 6(3), 1501873.
- [11] Li, Y., Meng, L., Yang, Y. M., Xu, G., Hong, Z., Chen, Q., ... & Li, Y. (2016). High-efficiency robust perovskite solar cells on ultrathin flexible substrates. *Nature communications*, 7, 10214.
- [12] Mao, L., Chen, Q., Li, Y., Li, Y., Cai, J., Su, W., ... & Chen, L. (2014). Flexible silver grid/PEDOT: PSS hybrid electrodes for large area inverted polymer solar cells. *Nano Energy*, 10, 259-267.
- [13] Kim, K., Kwon, H. C., Ma, S., Lee, E., Yun, S. C., Jang, G., ... & Moon, J. (2018). All-Solution-Processed Thermally and Chemically Stable Copper–Nickel Core–Shell Nanowire-Based Composite Window Electrodes for Perovskite Solar Cells. *ACS*

- applied materials & interfaces*, 10(36), 30337-30347.
- [14] Lee, E., Ahn, J., Kwon, H. C., Ma, S., Kim, K., Yun, S., & Moon, J. (2018). All-Solution-Processed Silver Nanowire Window Electrode-Based Flexible Perovskite Solar Cells Enabled with Amorphous Metal Oxide Protection. *Advanced Energy Materials*, 8(9), 1702182.
- [15] Wu, H., Kong, D., Ruan, Z., Hsu, P. C., Wang, S., Yu, Z., ... & Cui, Y. (2013). A transparent electrode based on a metal nanotrough network. *Nature nanotechnology*, 8(6), 421.
- [16] Lim, E. L., Yap, C. C., Jumali, M. H. H., Teridi, M. A. M., & Teh, C. H. (2018). A mini review: can graphene be a novel material for perovskite solar cell applications?. *Nano-micro letters*, 10(2), 27.
- [17] Luo, Q., Ma, H., Hou, Q., Li, Y., Ren, J., Dai, X., ... & He, H. (2018). All-carbon-electrode-based durable flexible perovskite solar cells. *Advanced Functional Materials*, 28(11), 1706777.
- [18] Bae, S., Kim, H., Lee, Y., Xu, X., Park, J. S., Zheng, Y., ... & Kim, Y. J. (2010). Roll-to-roll production of 30-inch graphene films for transparent electrodes. *Nature nanotechnology*, 5(8), 574.
- [19] Dong, H., Wu, Z., Jiang, Y., Liu, W., Li, X., Jiao, B., ... & Hou, X. (2016). A flexible and thin graphene/silver nanowires/polymer hybrid transparent electrode for optoelectronic devices. *ACS applied materials & interfaces*, 8(45), 31212-31221.
- [20] Deng, B., Hsu, P. C., Chen, G., Chandrashekar, B. N., Liao, L., Ayitimuda, Z., ... & Aisijiang, M. (2015). Roll-to-roll encapsulation of metal nanowires between graphene and plastic substrate for high-performance flexible transparent electrodes. *Nano*

- letters*, 15(6), 4206-4213.
- [21] Besleaga, C., Abramiuc, L. E., Stancu, V., Tomulescu, A. G., Sima, M., Trinca, L., ... & Svavarsson, H. G. (2016). Iodine migration and degradation of perovskite solar cells enhanced by metallic electrodes. *The journal of physical chemistry letters*, 7(24), 5168-5175.
- [22] Alotaibi, F., Tung, T. T., Nine, M. J., Coghlan, C. J., & Losic, D. (2018). Silver nanowires with pristine graphene oxidation barriers for stable and high performance transparent conductive films. *ACS Applied Nano Materials*, 1(5), 2249-2260.
- [23] Das, S., Pandey, D., Thomas, J., & Roy, T. (2019). The role of graphene and other 2D materials in solar photovoltaics. *Advanced Materials*, 31(1), 1802722.
- [24] HwanáKo, S. (2017). A dual-scale metal nanowire network transparent conductor for highly efficient and flexible organic light emitting diodes. *Nanoscale*, 9(5), 1978-1985.
- [25] Park, M., Cho, W., Lee, G., Hong, S. C., Kim, M. C., Yoon, J., ... & Choi, M. (2019). Highly Reproducible Large-Area Perovskite Solar Cell Fabrication via Continuous Megasonic Spray Coating of CH<sub>3</sub>NH<sub>3</sub>PbI<sub>3</sub>. *Small*, 15(1), 1804005.
- [26] Yoon, J., Sung, H., Lee, G., Cho, W., Ahn, N., Jung, H. S., & Choi, M. (2017). Superflexible, high-efficiency perovskite solar cells utilizing graphene electrodes: towards future foldable power sources. *Energy & Environmental Science*, 10(1), 337-345.
- [27] Hong, S., Lee, J., Kang, H., Kim, G., Kee, S., Lee, J. H., ... & Yu, K. (2018). High-efficiency large-area perovskite photovoltaic

modules achieved via electrochemically assembled metal-filamentary nanoelectrodes. *Science advances*, 4(8), eaat3604.

## Chapter 5.

### Conclusion

---

In this dissertation, allotropes of carbon were introduced and optimized to integrate into flexible perovskite solar cells to replace conventional high-temperature processed transporting layers and high-cost brittle electrode.

First, a flexible stable perovskite with no hysteresis utilizing  $C_{60}$  as an electron transporting layer was realized and its stability was tested. To stabilize the transporting layer that caused major hysteresis and fabrication failure,  $C_{60}$  replaced conventional  $TiO_2$  electron transporting layer and eliminated bathocuproine layer to balance the band alignment of each layer within the perovskite solar cell. As a result, the  $C_{60}$  based flexible perovskite performed with PCE of 16.0%. For both rigid and flexible substrate, the  $C_{60}$  based flexible perovskite solar cell exhibited excellent stability by showing no hysteresis at a rapid scanning rate. Additionally, the PEN-based flexible device showed its durability over bending conditions. The cell maintained its performance over 90% after 1000 cycles of bending test with a radius of curvature of 10 mm. This

study has set a new standard of stable flexible perovskite solar cell with promising results.

Second, a graphene-based hybrid electrode was realized to overcome the limitations of existing alternative transparent electrodes for flexible optical devices. The combination of graphene and Ag NW led a self-complementary condition that enhances each other's limitations with the help of amorphous Teflon backbone polymer layer. Graphene enlarged its size limitations by enhancing its conductivity with help of a super thin layer of Ag NW. Ag NW was able to protect its own layer with help of graphene to enhance its chemical stability over any chemicals including organic solvents. Both graphene and Ag NW are suitable for flexibility and showed similar transparency and conductivity as that of ITO. Unlike ITO, the transparency and conductivity of this hybrid electrode are controllable. The roughness of the hybrid electrode was very flat with under 5 nm of roughness rms. The surface treatment with PFN enhanced the surface compatibility with other chemicals. The hybrid electrode showed its compatibility in both spin-coating and megasonic spray deposition. This study has shown the potential of the graphene-based hybrid electrode and its accessibility to be integrated into other optical and energy-related

research area.

Overall the studies have shown the advantage over the most abundant material on earth, carbon. Carbon and its allotropes can replace major parts of perovskite solar cells excluding the active layer, perovskite. Its potential of stabilizing perovskite solar cell is expected to strengthen the possibility of the production of industrial flexible perovskite solar cell. Moreover, the introduction of a new hybrid electrode that can potentially replace ITO and stop the monopoly of indium price war should open a new area of studies with its superb flexibility.

## Acknowledgement

This work was supported by the Global Frontier R&D Program on Center for Multiscale Energy System funded by the National Research Foundation under the Ministry of Science, ICT, and Future Planning, Korea.

The research data of Chapter 3 are the result on the collaboration with Prof. Seong Min Kang. In addition, the research data of Chapter 3 have been published in Energy and Environmental science (*Energy Environ. Sci.*, 2016, **9**, 2262–2266). The research data of Chapter 4 are the result on the collaboration with Phillip Won. In addition, the research results of this chapter will be published in the academic journals.

I would like to thank my supervisor Prof. Mansoo Choi for their warm encouragement and helpful advices. I am also grateful to Dr. Jong-Kwon Lee and Prof. Min Seok Jang for their considerable guidance and encouragement. I would like to especially thank Phillip Won and Seung Chang Hong for their stimulating discussions and passionate contributions throughout this work. I also appreciate all of my laboratory members for their kind support, assistance and many helps.

# 유연 페로브스카이트 태양전지를 위한 탄소기반 기능성 물질의 응용

서울대학교 대학원 기계항공공학부

윤 희 태

## 요약

페로브스카이트 태양전지는 태양전지 산업의 후발주자이자 가장 최근 기술이 적용된 태양전지이다. 다양한 분야의 연구자들은 지난 몇 년 동안 큰 잠재력과 빠른 성장으로 이 신세대 태양전지의 발전에 관심을 기울였다. 기존의 실리콘 태양전지와는 달리, 페로브스카이트 태양전지는 유연한 기판을 응용하여 새로운 연구 분야를 열 수 있었다. 그러나 기존의 단단한 기판에서 유연 기판으로 이동하는 데는 물질적인 한계가 있었다. PEN과 같은 유연 기판은  $\text{TiO}_2$ 와 같은 기존 수송층의 고온 처리를 견딜 수 없었다. 또한 보편적으로 사용되는 투명 전극 인 ITO는 가격 상승등의 어려움을 겪고있다. 이 논문에서는 기존의 고온 처리된 수송층과 고비용의 유연 전극을 대체하기 위해 탄소의 동소체를 도입하여 유연한 페로브스카이트 태양전지에 통합하도록 최적화했다.

첫째, 전자 수송층으로서  $\text{C}_{60}$ 을 이용한 히스테리시스가 없는 유연하고 안정한 페로브스카이트를 실현하고 그 안정성을 시험 하였다. 주요 히스테리시스 및 장기적 효율 손실을 유발하는 수송층을

안정화시키기 위해,  $C_{60}$ 은 종래의  $TiO_2$  전자 수송층을 대체하고 BCP 층을 제거하여 페로브스카이트 태양전지 내의 각 층의 밴드 정렬의 균형을 조정하였다. 그 결과,  $C_{60}$  기반의 유연 페로브스카이트는 16.0 %의 광전변환효율을 보였다. 단단한 기판과 유연 기판 모두  $C_{60}$  기반의 유연 페로브스카이트 태양전지는 빠른 스캔 속도에서 히스테리시스를 나타내지 않아 우수한 안정성을 보였다. 또한, PEN 기반의 유연한 소자는 굽힘 조건에서 내구성을 보였다. 셀은 곡률 반경이 10 mm 인 1000번의 굴곡 테스트 후 90 % 이상의 성능을 유지했다. 이 연구는 고효율과 히스테리시스 없는 안정적 결과를 토대로 유연한 페로브스카이트 태양전지의 새로운 표준을 설정했다.

둘째, 그래핀 기반 하이브리드 전극은 기존의 유연한 광학 소자 용 투명 전극의 한계를 극복하기 위해 실현되었다. 그래핀과 은 나노와이어의 조합은 무정형 테플론 백본 폴리머 층의 도움으로 서로의 한계를 향상시키는 자기 보완 조건을 이끌어 냈다. 그래핀은 은 나노와이어의 초박막 층을 사용하여 전도성을 향상시킴으로써 크기 제한을 확대했다. 은 나노와이어는 유기 용매를 포함한 모든 화학 물질보다 화학 안정성을 향상시키기 위해 그래핀의 도움으로 자체 층을 보호 할 수 있었다. 그래핀과 은 나노와이어는 모두 유연성에 적합하며 ITO와 비슷한 투명성과 전도성을 보였다. ITO와는 달리 하이브리드 전극의 투명성과 전도성은 제어 가능하다. 하이브리드 전극의 거칠기는 5 nm 미만의 거칠기 rms로 매우 평탄했다. PFN을 이용한 표면 처리는 다른 화학 물질과의 표면 호환성을 향상 시켰다. 하이브리드 전극은 스핀 코팅 및 메가소닉 스프레이 증착 모두에서 호환성을 보였다. 이 연구는 그래핀 기반 하이브리드 전극의 가능성과 다른 광학 및 에너지 관련 연구 영역에 적용 될 수 있는 접근

가능성을 보여주었다.

전반적으로 이 연구는 지구상에서 가장 풍부한 탄소 물질에 대한 이점을 보여주었다. 탄소와 그 동종 원소는 활성층, 페로브스카이트를 제외한 페로브스카이트 태양전지의 주요 부분을 대체 할 수있다. 페로브스카이트 태양전지의 안정화 가능성은 산업용 유연한 페로브스카이트 태양전지의 생산 가능성을 강화시킬 것으로 기대된다. 더욱이, 잠재적으로 ITO를 대체하고 인듐 가격 전쟁의 독점을 막을 수 있는 새로운 하이브리드 전극의 도입은 탁월한 유연성으로 연구의 새로운 영역을 열어 줄 것이다.

**주요어:** 페로브스카이트 태양전지, 유연 소자, 탄소, 투명 전극, 히스테리시스, C<sub>60</sub>

**학번:** 2013-20689

## List of Publications

- [1] Lee, J., Sung, H., Jang, M., **Yoon, H.** and Choi, M. (2015). Reliable doping and carrier concentration control in graphene by aerosol-derived metal nanoparticles. *Journal of Materials Chemistry C*, 3(32), 8294-8299.
  
- [2] **Yoon, H.**, Kang, S. M., Lee, J.-K., & Choi, M. (2016). Hysteresis-free low-temperature-processed planar perovskite solar cells with 19.1% efficiency. *Energy & Environmental Science*, 9(7), 2262-2266.
  
- [3] Ahn, N., Kwak, K., Jang, M. S., **Yoon, H.**, Lee, B. Y., Lee, J.-K., Choi, M. (2016). Trapped charge-driven degradation of perovskite solar cells. *Nature communications*, 7, 13422.
  
- [4] Sung, H., Ahn, N., Jang, M. S., Lee, J. K., **Yoon, H.**, Park, N. G., & Choi, M. (2016). Transparent Conductive Oxide-Free Graphene-Based Perovskite Solar Cells with over 17% Efficiency. *Advanced Energy Materials*, 6(3), 1501873.